UNIVERSITY OF CALIFORNIA, SAN DIEGO

Electron dynamics in nanoscale systems

A dissertation submitted in partial satisfaction of the
requirements for the degree
Doctor of Philosophy

in

Physics

by

Neil G. Bushong

Committee in charge:

Professor Massimiliano Di Ventra, Chair
Professor Daniel Arovas
Professor Dimitri Basov
Professor Clifford Kubiak
Professor Ed Yu

2007

The dissertation of Neil G. Bushong is approved, and it is acceptable in quality and form for publication on microfilm:

Chair

University of California, San Diego

2007

To my wife, Dana

TABLE OF CONTENTS

LIST OF FIGURES

LIST OF TABLES

ACKNOWLEDGEMENTS

Over the course of carrying out the work described in this document, my wife Dana has provided me with a bedrock of love and support. And although I have not had the chance to see them as often as I would have liked, my parents and sister have also been a source of encouragement and strength.

It almost goes without saying that my advisor Massimiliano Di Ventra has provided me with a wealth of experience and direction. But in addition, he has been a source of infectious enthusiasm for the subject matter, which has been nearly as useful as his keen physical insight.

Much of the work described here was produced as a collaboration with my gifted colleagues Na Sai, Yuriy Pershin, Ryan Hatcher, and John Gamble. In addition, I would also like to acknowledge the help of Johan Lagerqvist, Mike Zwolak and Roberto D'Agosta. While I have not produced any specific publications with this latter group, a large portion of my professional and intellectual development has happened with their help.

Finally, I would like to thank my fellow students Ryan Baumbach and Kyle Campbell for being a daily source of interesting lunchtime discussions, some of which were even tangentially work-related.

Chapter 3 is in part a reprint of the material as it appears in Neil Bushong, Na Sai and Massimiliano Di Ventra, "Approach to steady-state transport in nanoscale conductors," *Nano Letters* **5**, 2569 (2005). The dissertation author was the primary investigator of this paper.

Chapter 4 is in part a reprint of the material as it appears in Na Sai, Neil Bushong, Ryan Hatcher and Massimiliano Di Ventra, "Microscopic current dynamics in nanoscale junctions," *Physical Review B* **75**, 115410 (2007). The dissertation author was a co-author of this paper.

Chapter 5 is in part a reprint of the material as it appears in Neil Bushong, John Gamble and Massimiliano Di Ventra, "Electron turbulence at nanoscale junctions," *Nano Letters* **7**, 1789 (2007). The dissertation author was the primary investigator

of this paper.

Chapter 6 is in part a reprint of the material as it appears in Neil Bushong, Yuriy Pershin and Massimiliano Di Ventra, "Turbulence-induced magnetic flux asymmetry at nanoscale junctions," *Physical Review Letters* **99** 226802 (2007). The dissertation author was the primary investigator of this paper.

VITA

2002	B. S., University of Florida
2002–2004	Teaching Assistant, Department of Physics, University of California, San Diego
2004	M. S., University of California, San Diego
2004–2007	Research Assistent, Department of Physics, University of California, San Diego
2007	Ph. D., University of California, San Diego

PUBLICATIONS

Neil Bushong and Massimiliano Di Ventra, "Current-induced effects in nanoscale conductors," in G. Cuniberti, G. Fagas and K Richter, editors, *Introducing Molecular Electronics*, Springer Verlag, Berlin, 2005.

Neil Bushong, Na Sai and Massimiliano Di Ventra, "Approach to steady-state transport in nanoscale conductors," *Nano Lett.* **5**, 2569 (2005).

Na Sai, Neil Bushong, Ryan Hatcher and Massimiliano Di Ventra, "Microscopic current dynamics in nanoscale junctions," *Phys. Rev. B* **75**, 115410 (2007).

Neil Bushong, John Gamble and Massimiliano Di Ventra, "Electron turbulence at nanoscale junctions," *Nano Lett.* **7**, 1789 (2007).

Neil Bushong, Yuriy Pershin and Massimiliano Di Ventra, "Turbulence-induced magnetic flux asymmetry at nanoscale junctions," *Phys. Rev. Lett.* **99**, 226802 (2007).

Neil Bushong and Massimiliano Di Ventra, "The decay of excited He from Stochastic Density-Functional Theory: a quantum measurement theory interpretation," in preparation.

ABSTRACT OF THE DISSERTATION

Electron dynamics in nanoscale systems

by

Neil G. Bushong
Doctor of Philosophy in Physics

University of California San Diego, 2007

Professor Massimiliano Di Ventra, Chair

In this dissertation we discuss the dynamical behavior of electrons on the nanoscopic scale. We begin by presenting a view of electron transport which is an alternative to that due to Landauer, in which the flow of electrons across a junction is framed as the discharge of a large but finite capacitor. The benefit of this construction is that time-dependent calculations can be framed in a conceptually simple and well-defined way. We characterize the conductance of a quasi-one-dimensinal chain of gold atoms, as well as a quantity which is similar to the distribution functions of classical statistical mechanics. We go on to the quasi-two-dimensional case and characterize the flow patterns of electrons emerging from a nanoscopic junction. We discuss the dynamic angular pattern of electron flow, as well as the movement of charge at the surface of the electrodes near the junction.

We continue by considering the hydrodynamic form of the many-body Schrödinger equation and demonstrate that the electron liquid develops turbulent eddy-like structures in experimentally attainable regimes. We provide the demonstration using both an ab-initio formalism, as well as an approximate Navier-Stokes calculation. We go on to describe an experiment whereby the turbulence of the electron liquid could be detected through the use of a Superconducting Quantum Interference Device (SQUID), by measuring the asymmetry in the magnetic flux

produced as a result of current flow near the nanoscopic junction. In addition, we characterize the turbulent eddies by considering the velocity correlation tensor.

Finally, we discuss the stochastic extension to current density functional theory and demonstrate the decay of a Helium atom which is effectively coupled to an external reservoir. We demonstrate the utility of the stochastic Schrödinger formalism as compared to the master equation approach, and discuss the relevance of the stochastic Shrödinger equation to quantum measurement theory.

1

Introduction

Density functional theory [1, 2] is an accurate and practical theoretical tool which can be used to study systems of many interacting electrons on the nanoscale. For example, one can use potentials extracted from density functional theory in order to describe electron transport through a nanoscopic junction [3–12]. However, most transport studies which have been conducted to date have concentrated on the static case, where the current density is completely fixed in time, and dynamical effects are neglected. Those studies which have been time-dependent [13–22] have suffered from the necessity of specifying the time-dependent distribution of electron charge and momentum at the boundaries. In this dissertation we will describe an approach to electron transport which avoids this difficulty by considering a finite-system approach. The method is inherantly time-dependent, but can still be used to extract static quantities such as the conductance. We will describe phenomena which are inaccessible to static calculations even in principle, and discuss how they may be measured experimentally. Finally, we will discuss how a dynamically-evolving nanoscopic system may be coupled to a bath on a stochastic basis, so that energy may be exchanged between the system and its environment.

We will begin in Chapter 2 by reviewing general background material which may be useful for the reader. We will describe the motivation for static density functional theory, and discuss the Hohenberg-Kohn theorem and the relationship

between fictional single-particle Kohn-Sham states and the true many-body density. We will go on to discuss the static description of electron transport using the Landauer approach, in which one considers an system connected to two reservoirs. Finally, we will present an overview of time-dependent density functional theory, as well as time-dependent current density functional theory, which includes hydrodynamic terms which will be particularly relevant later in Chapters 5 and 6.

We go on in Chapter 3 to show, using a tight-binding model and time-dependent density-functional theory, that a quasi-steady state current can be established dynamically in a finite nanoscale junction without any inelastic effects. This is simply due to the geometrical constriction experienced by the electrons as they propagate through the junction. We also show that in this closed non-equilibrium system two local electron occupation functions can be defined on each side of the nanojunction which approach Fermi distributions with increasing number of atoms in the electrodes. The resultant conductance and current-voltage characteristics at quasi-steady state are in agreement with those calculated within the static scattering approach.

In Chapter 4, we will present a numerical study of microscopic current flow dynamics in nanoscale quantum point contacts using the approach described in Chapter 3, combining a closed and finite geometry with time-dependent density functional theory. Using both atomic and jellium model calculations, we will show that the time evolution of the current flow exhibits several noteworthy features, including nonlaminar flow, and dominating lateral flows near the electrode surfaces. We will attribute these features to the presence of the lattice and the surface charges that are dynamically formed at the junction-electrode interfaces. In addition, our results support the notion that the quantum system undergoing transport exhibits characteristics similar to a classical liquid.

In Chapter 5, we will note that electron transport through a nanostructure can be characterized in part using concepts from classical fluid dynamics. It is thus natural to ask how far the analogy can be taken, and whether the electron liquid can exhibit nonlinear dynamical effects such as turbulence. We therefore will

present an *ab-initio* study of the electron dynamics in nanojunctions which reveals that the latter indeed exhibits behavior quite similar to that of a classical fluid. In particular, we will find that a transition from laminar to turbulent flow occurs with increasing current, corresponding to increasing Reynolds numbers. These results reveal unexpected features of electron dynamics and shed new light on our understanding of transport properties of nanoscale systems.

Chapter 6 will continue the analysis of turbulence in the electron liquid by showing that such an effect leads to an asymmetric current-induced magnetic field on the two sides of an otherwise symmetric junction. We will propose that measuring the fluxes ensuing from these fields across two surfaces placed at the two sides of the junction would provide direct and non-invasive evidence of the transition from laminar to turbulent electron flow. The flux asymmetry is predicted to first increase, reach a maximum and then decrease with increasing current, i.e., with increasing amount of turbulence.

Finally, in Chapter 7, we will make use of the recent extension to time-dependent current-density functional theory which includes the dynamical interaction of quantum systems with external environments. We will show that such a theory allows us to study a fundamentally important class of phenomena previously inaccessible by standard density-functional methods: the decay of excited systems. As an example we study the decay of an ensemble of excited He atoms, and discuss these results in the context of quantum measurement theory.

A note about units

In this dissertation, we will use atomic units, in which $\hbar = |e| = a_0 = m_e = \frac{1}{4\pi\epsilon_0} = 1$.

2

Density functional treatments of electron dynamics

2.1 The many-particle Shrödinger equation

The dynamical behavior of a group of interacting electrons is governed by the Schrödinger equation, which is given by

$$\hat{H}|\Psi\rangle = \mathrm{i}\frac{\mathrm{d}}{\mathrm{d}t}|\Psi\rangle\,, \tag{2.1}$$

where the Hamiltonian H is given by

$$\hat{H} = \sum_i \frac{\hat{p}_i^2}{2} + \frac{1}{2}\sum_{i\neq j}\frac{1}{|\hat{\mathbf{r}}_i - \hat{\mathbf{r}}_j|} + \hat{V}\,. \tag{2.2}$$

Here, $\hat{\mathbf{r}}_i$ and $\hat{\mathbf{p}}_i$ are the position and momentum operators for a particular electron i, and $\hat{V}$ denotes the local potential due to the "background" potential, such as a lattice of atomic nuclei. In addition, electrons obey the symmetry that, upon the interchange of two electrons, the sign of the many-electron wavefunction $|\Psi\rangle$ is reversed. This symmetry requirement may be satisfied by regarding $|\Psi\rangle$ as a linear combination of Fock states $|\alpha_1, \alpha_2, \ldots, \alpha_N\rangle$; in the position basis, each Fock state can be written as a Slater determinant:

$$\psi_{\alpha_1,\alpha_2,\ldots,\alpha_N}(\mathbf{r}_1,\sigma_1;\mathbf{r}_2,\sigma_2;\ldots,\mathbf{r}_N,\sigma_N) = \frac{1}{\sqrt{N!}}\det\left[\phi_{\alpha_i}(\mathbf{r}_j,\sigma_j)\right]\,, \tag{2.3}$$

where σ labels the electron spin (i.e., "up" or "down"). For example, for a system consisting of two electrons, with $\{\phi_a, \phi_b, \phi_c\}$, as elements of a single-particle basis set, one allowed wavefunction might be

$$\begin{aligned}\Psi(\mathbf{r}_1,\sigma_1;\mathbf{r}_2,\sigma_2) &= A\psi_{a,b}(\mathbf{r}_1,\sigma_1;\mathbf{r}_2,\sigma_2) + B\psi_{b,c}(\mathbf{r}_1,\sigma_1;\mathbf{r}_2,\sigma_2) + C\psi_{c,a}(\mathbf{r}_1,\sigma_1;\mathbf{r}_2,\sigma_2) \\ &= \frac{A}{\sqrt{2}}\Big(\phi_a(\mathbf{r}_1,\sigma_1)\phi_b(\mathbf{r}_2,\sigma_2) - \phi_b(\mathbf{r}_1,\sigma_1)\phi_a(\mathbf{r}_2,\sigma_2)\Big) \\ &+ \frac{B}{\sqrt{2}}\Big(\phi_b(\mathbf{r}_1,\sigma_1)\phi_c(\mathbf{r}_2,\sigma_2) - \phi_c(\mathbf{r}_1,\sigma_1)\phi_b(\mathbf{r}_2,\sigma_2)\Big) \\ &+ \frac{C}{\sqrt{2}}\Big(\phi_c(\mathbf{r}_1,\sigma_1)\phi_a(\mathbf{r}_2,\sigma_2) - \phi_a(\mathbf{r}_1,\sigma_1)\phi_c(\mathbf{r}_2,\sigma_2)\Big)\,,\end{aligned} \tag{2.4}$$

where A, B and C are coefficients such that $|A|^2 + |B|^2 + |C|^2 = 1$. Clearly, interchanging $\mathbf{r}_1, \sigma_1$ and $\mathbf{r}_2, \sigma_2$ in the above expression is equivalent to multiplying the wavefunction by a factor of -1.

In principle, it is possible to numerically solve the many-electron Shrödinger equation. In practice, however, for problems involving more than one Slater determinant, the problem rapidly becomes intractable as the number of electrons N increases because, in general, one must keep track of X^N different terms, where X is the number of elements in the basis set. This illustrates the utility of density functional theory (DFT), which reduces the problem to one of *noninteracting* electrons. In that case, one must only keep track of only $X \times N$ terms, which is a much more manageable level of complexity.

2.2 Static density functional theory

The central insight of density functional theory is that there is a mapping between the Hamiltonian (2.2) and the ground state value of the density $n(\mathbf{r})$, where $n(\mathbf{r})$ is the expectation value density operator $\hat{n}(\mathbf{r})$:

$$\hat{n}(\mathbf{r}) = \sum_{i=1}^{N} \delta(\mathbf{r} - \hat{\mathbf{r}}_i)\,. \tag{2.5}$$

While a particular potential $\hat{V}$ may lead to multiple (degenerate) ground state densities, no two different potentials will ever give the same ground state density. (Here we discount potentials that differ merely by a constant factor.) Therefore, given the ground state density, we can in principle infer the Hamiltonian, and therefore infer anything else about the system we care to know.

The proof of this statement is rather straightforward, and proceeds by *reductio ad absudum* [1]. Consider two different Hamiltonians $\hat{H}$ and $\hat{H}'$, with ground state wavefunctions $|E\rangle$ and $|E'\rangle$, which correspond to the different eigen-energies E and E'.[1] If we assume that the two Hamiltonians share the same ground state density $n(\mathbf{r})$, so that $n(\mathbf{r}) = \langle E|\hat{n}(\mathbf{r})|E\rangle = \langle E'|\hat{n}(\mathbf{r})|E'\rangle$, then by the Rayleigh-Ritz variational principle [23] we know that

$$E' = \langle E'|\hat{H}'|E'\rangle < \langle E|\hat{H}'|E\rangle = \langle E|(\hat{H} + \hat{V}' - \hat{V})|E\rangle \,. \tag{2.6}$$

Since $\hat{V}$ is local, we can write

$$\hat{V} = \sum_{i=1}^{N} \int \mathrm{d}\mathbf{r}\, V(\mathbf{r})\delta(\mathbf{r} - \mathbf{r_i}) = \int \mathrm{d}\mathbf{r}\, V(\mathbf{r})\hat{n}(\mathbf{r}) \,. \tag{2.7}$$

Hence,

$$E' < E + \int \mathrm{d}\mathbf{r}\, (V'(\mathbf{r}) - V(\mathbf{r}))\, n(\mathbf{r}) \,. \tag{2.8}$$

However, we can go through this logic again, exchanging primed and unprimed quantities, and show that

$$E < E' + \int \mathrm{d}\mathbf{r}\, (V(\mathbf{r}) - V'(\mathbf{r})) \,. \tag{2.9}$$

Adding equations (2.8) and (2.9), we have

$$E + E' < E + E' \,, \tag{2.10}$$

which is a contradiction. Therefore, our assumption that two different Hamiltonians can yield the same ground state density must be incorrect.

[1] Note that $|E\rangle \neq |E'\rangle$, or we would have $(E - E')|E\rangle = (\hat{H} - \hat{H}')|E\rangle = (\hat{V} - \hat{V}')|E\rangle$, which implies that V and V' merely differ by a constant, counter to our earlier statement that we discount potentials which are trivially related in this way.

Hence, given a local potential V, the ground state energy functional E is minimized by the ground state density.[2] We can decompose this functional into two parts,

$$E[n] = \int \mathrm{d}\mathbf{r}\, V(\mathbf{r}) n(\mathbf{r}) + F[n]\,, \tag{2.11}$$

where $F[n]$ is a universal functional of the density only. Since $E[n]$ is extremized at the ground state density, so that $\delta E[n]/\delta n(\mathbf{r}) = 0$, equation (2.11) implies that, at the ground state density,

$$\frac{\delta F[n(\mathbf{r})]}{\delta n(\mathbf{r})} = -V(\mathbf{r})\,. \tag{2.12}$$

We will make use of this fact in a moment.

We can simplify the full interacting many-body Hamiltonian by decomposing $F[n]$ into

$$F[n] = T_{\mathrm{s}}[n] + E_{\mathrm{H}}[n] + E_{\mathrm{xc}}[n]\,. \tag{2.13}$$

Here, $T_{\mathrm{s}}[n]$ is defined to the the kinetic energy functional that minimizes $F[n]$ for a system of *noninteracting* electrons whose density is n, and the Hartree energy E_{H} is given by

$$E_{\mathrm{H}}[n] = \frac{1}{2}\int \mathrm{d}\mathbf{r} \int \mathrm{d}\mathbf{r}' \frac{n(\mathbf{r}) n(\mathbf{r}')}{|\mathbf{r} - \mathbf{r}'|}\,. \tag{2.14}$$

The remainder, $E_{\mathrm{xc}}[n]$, is called the exchange-correlation energy functional, and is defined by equation (2.13).

With this definition, we see that equation (2.12) implies that

$$\frac{\delta T_{\mathrm{s}}[n]}{\delta n} = -V(\mathbf{r}) - \frac{\delta E_{\mathrm{H}}[n]}{\delta n} - \frac{\delta E_{\mathrm{xc}}[n]}{\delta n}\,. \tag{2.15}$$

If we define

$$V_{\mathrm{KS}}(\mathbf{r}) \equiv V(\mathbf{r}) + V_{\mathrm{H}}(\mathbf{r}) + V_{\mathrm{xc}}(\mathbf{r})\,, \tag{2.16}$$

[2]The minimization needs to be carried out such that the density corresponds to wavefunctions whose sign is changed upon the interchange of two electrons. One way to accomplish this is to separate the minimization into two steps: in the first step, the density is fixed, and the energy is minimized with respect to admissible wavefunctions, while in the second step, the energy is minimized over that set of densities [24, 25].

where $V_{\rm H}(\mathbf{r}) \equiv \frac{\delta E_{\rm H}[n]}{\delta n}$ and $V_{\rm xc}(\mathbf{r}) \equiv \frac{\delta E_{\rm xc}[n]}{\delta n}$, then

$$\frac{\delta T_{\rm s}[n]}{\delta n} = -V_{KS}(\mathbf{r})\,. \tag{2.17}$$

This is equation (2.12) for the special case of noninteracting electrons under the influence of a potential $V_{\rm KS}(\mathbf{r})$. Thus, if we want to find the ground state density of a system of N interacting electrons subject to a potential $V(\mathbf{r})$, we can just find the ground state density for a noninteracting system of N electrons which are subject to a potential $V_{\rm KS}(\mathbf{r})$. In the position basis, this amounts to solving

$$\left[-\frac{1}{2}\nabla^2 + V(\mathbf{r}) + V_{\rm H}(\mathbf{r}) + V_{\rm xc}(\mathbf{r})\right]\phi_i(\mathbf{r},\sigma) = \varepsilon_i\phi_i(\mathbf{r},\sigma)\,. \tag{2.18}$$

The quantity in brackets is called the Kohn-Sham Hamiltonian Each ε_i is a Kohn-Sham eigenvalue, and ϕ_i is the corresponding Kohn-Sham eigenstate.[3] The density is then given by[4]

$$n(\mathbf{r}) = \sum_{i=1}^{N}\sum_{\sigma}|\phi_i(\mathbf{r},\sigma)|^2\,. \tag{2.19}$$

Note that, while the ground state density can be obtained by minimizing

$$E^{(0)}[n] = T_{\rm s}[n] + \int \mathrm{d}\mathbf{r}\, V_{\rm KS}(\mathbf{r})n(\mathbf{r})\,, \tag{2.20}$$

this does not give us the true energy of the interacting system. That is, $E^{(0)}[n] \neq E[n]$, even though they are both extremized for the same density $n(\mathbf{r})$. However, given the ground state density, we can still infer $E[n]$ using the Kohn-Sham formalism in a simple way. Since

$$T_{\rm S}[n] + \int \mathrm{d}\mathbf{r}\, V_{\rm KS}(\mathbf{r})n(\mathbf{r}) = \sum_{i=1}^{N}\varepsilon_i\,, \tag{2.21}$$

[3]Note that the Kohn-Sham states are not the "real" eigenstates of the system. They are only physically significant in that their summed density gives the true many-body density.

[4]One can use equation (2.19) to calculate the density for a system of non-interacting electrons if the ground state can be given as a single Slater determinant. This is usually true, although it is possible to construct an example of a "normal-looking" density for which no ground-state single-determinant wavefunction exists [25, 26]. Densities which correspond to a ground-state single-determinant wavefunction are called "pure-state V-representable."

equation (2.13) implies

$$F[n] = \sum_{\alpha=1}^{N} \varepsilon_\alpha - \int \mathrm{d}\mathbf{r}\, V_{\mathrm{KS}}(\mathbf{r}) n(\mathbf{r}) + E_{\mathrm{H}}[n] + E_{\mathrm{xc}}[n]\,. \tag{2.22}$$

This, together with equations (2.11), (2.14) and (2.16), implies that the total energy is given by

$$E[n] = \sum_{\alpha=1}^{N} \varepsilon_\alpha - \frac{1}{2} \int \mathrm{d}\mathbf{r}\, n(\mathbf{r}) \int \mathrm{d}\mathbf{r}'\, \frac{n(\mathbf{r}')}{|\mathbf{r} - \mathbf{r}'|} - \int \mathrm{d}\mathbf{r}\, n(\mathbf{r}) V_{\mathrm{xc}}(\mathbf{r}) + E_{\mathrm{xc}}[n]\,. \tag{2.23}$$

Note that the Hamiltonian is a functional of the density, and the density itself comes from the eigenvectors of the Hamiltonian. The problem is thus a self-consistent one. One typically finds a solution by starting with a guess for the density, constructing the corresponding Hamiltonian, finding the resultant density, and repeating the process until the density stops changing by an appreciable amount. The density of course is not guaranteed to converge, but one can encourage convergence by using a mixture of "old" and "new" densities during each iteration, a process called simple mixing [27]. More sophisticated mixing schemes are also available [28, 29].

We began with the problem of finding the ground state for a system of interacting electrons in a local potential V, and argued that this problem rapidly becomes intractable. We then cast the problem into a much simpler problem of *noninteracting* electrons interacting in a potential V_{KS}. However, we do not know the potential V_{KS}; in particular, we do not know V_{xc}. In effect, we have not made any progress in solving the problem at hand; we have merely put all the difficulty of the problem into finding V_{xc}. The utility of density functional theory lies in the fact that approximations for V_{xc} have been formulated which reproduce experimental results (such as molecular bond lengths or total energies) with reasonable accuracy.

In particular, the Local Density Approximation (LDA) has seen wide use. We decompose V_{xc} into

$$V_{\mathrm{xc}}(\mathbf{r}) = V_{\mathrm{x}}(\mathbf{r}) + V_{\mathrm{c}}(\mathbf{r})\,, \tag{2.24}$$

where the exchange potential $V_{\rm x}$ takes into account the effect of the exchange symmetry, and $V_{\rm c}$ is (again) defined by equation (2.24). The LDA proceeds by considering $V_{\rm x}$ for the case of a homogeneous electron liquid, and can be calculated exactly. It turns out to be[5] [2, 32]

$$V_{\rm x}^{\rm LDA}(\mathbf{r}) = -\left(\frac{3}{\pi}n(\mathbf{r})\right)^{\frac{1}{3}} . \tag{2.25}$$

The functional we will use for $V_{\rm c}$ in this dissertation was calculated by Ceperley and Alder [33] for a uniform electron gas using Monte Carlo techniques, and was parameterized by Perdew and Zunger [34]. The function itself is given in Appendix A.

It is interesting to note that the LDA seems to work better than one might have any right to expect. It has been argued [25] that part of the reason for this has to do with the fact that the true ground state density satisfies the sum rule

$$\int \mathrm{d}\mathbf{r}' \left[g(\mathbf{r},\mathbf{r}') - 1\right] n(\mathbf{r}') = -1 \,, \tag{2.26}$$

where

$$g(\mathbf{r},\mathbf{r}') \equiv \frac{1}{n(\mathbf{r})n(\mathbf{r}')} \left\langle \sum_{i\neq j} \delta(\mathbf{r}-\mathbf{r}_i)\delta(\mathbf{r}'-\mathbf{r}_j) \right\rangle \tag{2.27}$$

is the pair correlation function, and gives the normalized probability of finding an electron at $\mathbf{r}$ and one at $\mathbf{r}'$ simultaneously. The LDA satisfies (2.26) automatically. Initial attempts to provide gradient-corrected terms to $V_{\rm xc}$ did not yield improved accuracy with respect to experiment, in part due to the fact that they did not respect the sum rule (2.26).[6]

[5] The Dirac LDA is now called "the" LDA, but another local density functional also exists, which is due to Slater [30] and differs by the Dirac functional by a factor of 3/2. Slater's functional is derived from the LDA exchange potential, while Dirac's is derived from the LDA energy [31].

[6] A popular gradient-dependent exchange-correlation potential which respects this sum rule is called the Generalized Gradient Approximation (GGA); in particular, one parameterization called PBE [35] has become quite popular, although we will not make use of it in this dissertation.

2.3 The scattering approach to nanoscopic electron transport

An experimentalist who wishes to study electron transport does so by putting an object (called the junction, or the sample) in contact with two electrodes. He or she then applies a bias across the electrodes, so that current flows across the junction. At this point, the experimentalist may measure the conductance of the junction, the noise properties, the local heating of the junction, or any other quantity of interest. If the junction is of nanoscopic dimensions (that is, if the length scale of the junction is comparable to the size of individual atoms), much of the difficulty of the process may lie in physically positioning the sample between the electrodes.

A theoretician seeking to describe electron transport is faced with different difficulties. The junction and the apparatus maintaining a bias are of wildly different length scales. Furthermore, the junction and the electrodes are not in equilibrium. (If they were, the electrons would not exhibit a net flow from one side to the other, by definition.) We are thus concerned with an extended, non-equilibrium system.

2.3.1 The Landauer picture

One possible avenue of attack is to explicitly treat only the junction and a portion of the electrodes near to the junction. The rest of the electrodes are then treated as infinite reservoirs, which are connected to the system at its edges. (See panel (a) of Figure 2.1.) This picture forms the basis of the Landauer approach to electron transport [36].

Panel (b) of Figure 2.1 schematically shows the system in the energy basis. The left and right electrodes are each in thermal equilibrium, with Fermi energies $E_{\mathrm{f}}^{\mathrm{L}}$ and $E_{\mathrm{f}}^{\mathrm{R}}$, respectively. (We are only considering the case where the temperature is zero, so that the Fermi distributions are simple step functions.) Applying a bias has the effect of shifting one electrode's energy states higher than those of the

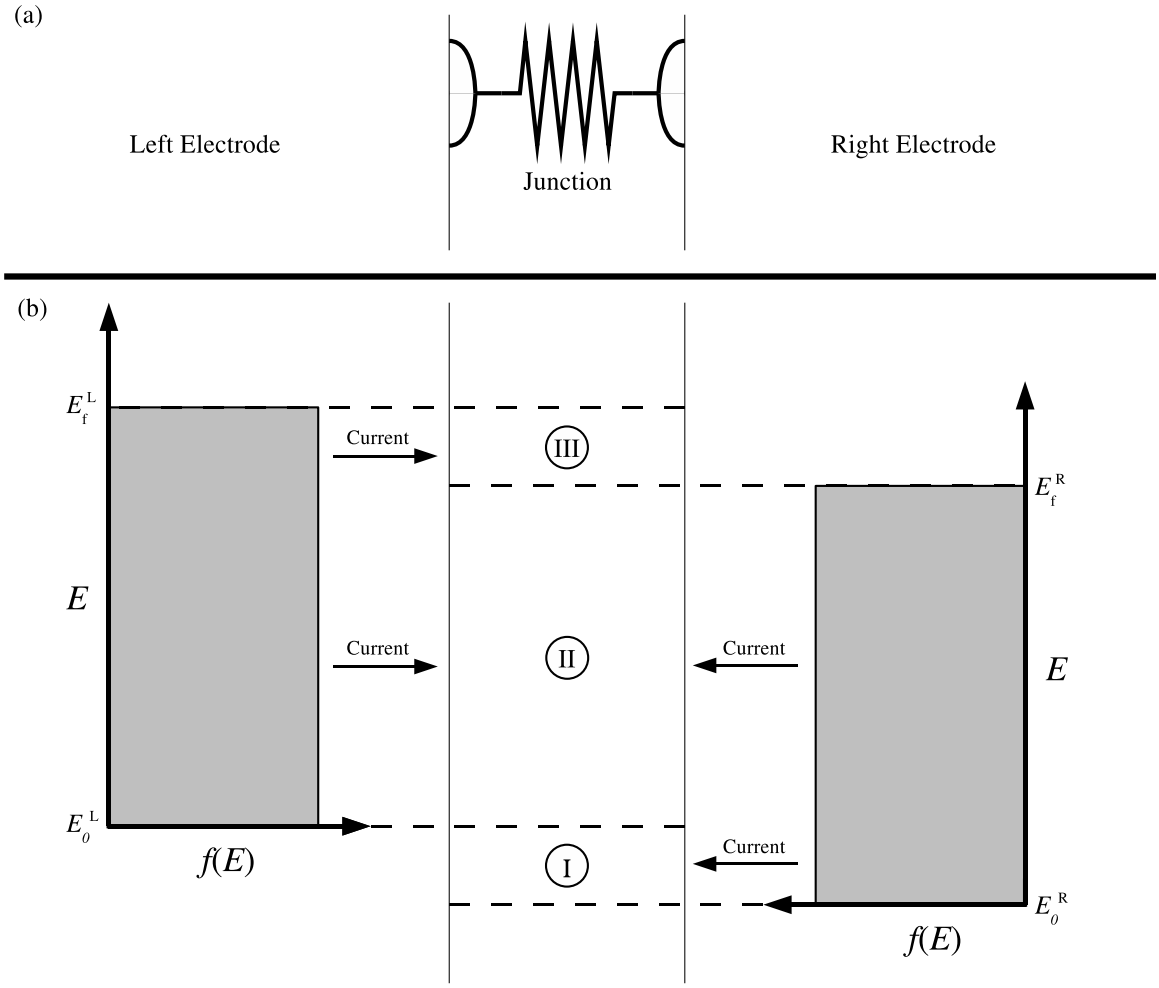

Figure 2.1 *Panel (a):* A system consisting of a resistive junction and a portion of the electrodes. The two semi-infinite electrodes are connected to the system at the boundaries. *Panel (b):* Depiction of transport in the Landauer picture, in the energy basis. The left and right electrodes are each in thermal equilibrium, with Fermi energies $E_{\rm f}^{\rm L}$ and $E_{\rm f}^{\rm R}$, respectively. (We have plotted the Fermi distributions "sideways," so that energy is plotted on the vertical axis, and occupation is plotted horizontally.) The applied bias is given by $V_{\rm B} = E_{\rm f}^{\rm L} - E_{\rm f}^{\rm R}$. See text for details.

other electrode; hence, the applied bias is equal to the difference in Fermi energies, so that $V_{\mathrm{B}} = E_{\mathrm{f}}^{\mathrm{L}} - E_{\mathrm{f}}^{\mathrm{R}}$.

We can identify three different ranges in energy, which we denote by Regions I, II and III. (See Figure 2.1(b).) We will first consider Region II, which consists of energy states with energy E such that $E_0^{\mathrm{L}} < E < E_{\mathrm{f}}^{\mathrm{R}}$, where E_0^{L} corresponds to the lowest-energy state in the left electrode. In Region II, electrons are available to flow both from the left electrode to the right electrode, as well as from the right electrode to the left electrode. The current flowing from the left to the right exactly cancels the current flowing from the right to the left, and so the net contribution to the total current from Region II is zero. (Even if the current did not cancel, there are no unoccupied states on either side which could accept electrons.)

Next, let us consider Region I, which consists of energy states with energy $E_0^{\mathrm{R}} < E < E_0^{\mathrm{L}}$, where E_0^{R} is defined analogously to E_0^{L}. Here, there are electronic states in the right electrode which can supply electrons; however, there are no states on the left to accept electrons. (By definition, E_0^{L} corresponds to the lowest energy state on the left.) Therefore, no current can flow, and the contribution to the total current from Region I is also zero.

However, in Region III, which is defined by energies $E_{\mathrm{f}}^{\mathrm{R}} < E < E_{\mathrm{f}}^{\mathrm{L}}$, the net current is nonzero. There exist occupied electronic states on the left, as well as unoccupied states on the right. Therefore, electrons can flow from the left to the right, yielding a nonzero total current.[7]

Therefore, one can infer the total current by summing the contribution to the current due to electrons with a range of energies corresponding to Region III. One option is to calculate the transmission coefficient T of an electron with energy E, with the total current being given by the amount of transmitted electrons in Region III; that is, $I \propto \int_{E_{\mathrm{f}}^{\mathrm{L}}}^{E_{\mathrm{f}}^{\mathrm{R}}} \mathrm{d}E\, T(E)$. A similar option, which we will describe in the next section, is to directly calculate the current density from the electronic

[7]Clearly, at zero bias, $E_{\mathrm{f}}^{\mathrm{L}} = E_{\mathrm{f}}^{\mathrm{R}}$, so that regions I and III disappear. Thus, at zero bias, Region II is all that remains; left-moving current is exactly cancelled by right-moving current, giving us zero net current, as expected.

wavefunctions.

2.3.2 The Lippmann-Schwinger equation applied to transport

In the Landauer picture, one can view the movement of electrons across a junction as a scattering problem.[8] The electrons are incident upon the junction with some distribution of momenta, and one infers the change in the wavefunction as a result of the presence of the junction.

Because many nanoscopic junctions of physical interest involve multiple interacting electrons, it is natural to take a density functional approach. The total density will arise from multiple Kohn-Sham states, each of which scatter off of a potential which is a functional of the density. Intuitively, this approach makes sense; however, it is worth noting that the Hohenberg-Kohn theorem is only valid for closed systems in the ground state. There is no rigorous theorem proving that it is valid to use the Kohn-Sham formalism in an open, non-equilibrium problem.

We begin by calculating the wavefunctions of the bare electrodes, without the junction. Since the system is translationally invariant in the directions parallel to the electrode surface, the bare-electrode problem is effectively one-dimensional. We separate the stationary states of the Kohn-Sham Hamiltonian for the bare electrodes $\Psi^0_{E\mathbf{K}_\parallel}$ into a product of transverse and parallel wavefunctions, so that

$$\Psi^0_{E\mathbf{K}_\parallel}(\mathbf{r}) = \mathrm{e}^{\mathrm{i}\mathbf{K}_\parallel\cdot\mathbf{R}} u_{E\mathbf{K}_\parallel}(z)\,, \tag{2.28}$$

where $\mathbf{K}_\parallel$ is the momentum of the plane wave parallel to the surface of the electrodes, $\mathbf{R}$ is the position parallel to the surface of the electrodes, z is the longitudinal position, and E is the energy. Given a Kohn-Sham Hamiltonian H and a transverse wave vector with magnitude $|\mathbf{K}_\parallel|$, we can find E and $u_{E\mathbf{K}_\parallel}$ by directly diagonalizing H. In keeping with the discussion in section 2.3.1, we will find that

[8] The approach we will describe in this section corresponds to that of Ref. 4, although there are a wealth of other theoretical studies whose approaches are extremely similar [3–12].

$u_{E\mathbf{K}_\parallel}$ will have a different qualitative character depending on whether E is in region I, II or III. For example, in Region III, the functions $u_{E\mathbf{K}_\parallel}(z)$ satisfy

$$u_{E\mathbf{K}_\parallel}(z) = (2\pi)^{3/2} k_{\mathrm{R}}^{-1/2} \times \begin{cases} \mathrm{e}^{\mathrm{i}k_{\mathrm{R}}z} + R\mathrm{e}^{\mathrm{i}k_{\mathrm{R}}z} & \text{for } z \to \infty \\ T\mathrm{e}^{-\mathrm{i}k_{\mathrm{L}}z} & \text{for } z \to -\infty\,, \end{cases} \tag{2.29}$$

where R and T are constant coefficients.

Next, we add the scattering potential V_{sc}. If we define $n^0(\mathbf{r})$ to be the density for the bare electrodes, and we define $n(\mathbf{r})$ to be the total density in the complete system which includes the electrodes (the "dressed" electrodes), then we can construct V_{sc} as the *change* in the total Kohn-Sham potential as a result of the change in total density due to the presence of the junction. We have

$$V_{\mathrm{sc}}(\mathbf{r},\mathbf{r}') = V_{\mathrm{ps}}(\mathbf{r},\mathbf{r}') + \left[V_{\mathrm{xc}}[n(\mathbf{r})] - V_{\mathrm{xc}}[n^0(\mathbf{r})] + \int \mathrm{d}\mathbf{r}'' \frac{n(\mathbf{r}'') - n^0(\mathbf{r}'')}{|\mathbf{r}-\mathbf{r}''|}\right]\delta(\mathbf{r}-\mathbf{r}')\,; \tag{2.30}$$

that is, V_{sc} is the sum of a local part and a nonlocal part. The local part (i.e., the second term on the right-hand side) is simply the difference of the Kohn-Sham potentials for the bare and dressed electrodes. The operator V_{ps} denotes a sum of pseudopotentials [37], and describes the effect of the atomic nuclei and core electrons for atoms in the junction.

Thus, in order to describe the change in the electronic wavefunctions as a result of the junction, we solve the time-independent Shrödinger equation in Lippmann-Schwinger form,

$$\Psi_{E\mathbf{K}_\parallel}(\mathbf{r}) = \Psi^0_{E\mathbf{K}_\parallel}(\mathbf{r}) + \int \mathrm{d}^3\mathbf{r}' \int \mathrm{d}^3\mathbf{r}''\, G^0_E(\mathbf{r},\mathbf{r}') V(\mathbf{r}',\mathbf{r}'') \Psi_{E\mathbf{K}_\parallel}(\mathbf{r}'')\,, \tag{2.31}$$

where $G^0_E(\mathbf{r},\mathbf{r}')$ is the Green's function.[9] Note that, for the dressed electrodes, there may be electronic states with energies *below* Region I. These are truly bound states, with wavefunctions localized in the junction, and they can be found by directly diagonalizing the Hamiltonian of the dressed electrodes.

[9]The form of the Green's function in the plane wave basis is given in Ref. 4.

The total current density for the dressed electrodes is

$$\mathbf{j}(\mathbf{r}) = -2\int_{E_0^{\mathrm{L}}}^{E_0^{\mathrm{R}}} \mathrm{d}E \int \mathrm{d}^2\mathbf{K}_\parallel \mathrm{Im}\left\{[\Psi_{E\mathbf{K}_\parallel}(\mathbf{r})]^* \nabla \Psi_{E\mathbf{K}_\parallel}(\mathbf{r})\right\} , \tag{2.32}$$

where the integral over $\mathbf{K}_\parallel$ is for $|\mathbf{K}_\parallel| < \sqrt{2[E - E_0^{\mathrm{R}}]}$. Note that the current density between the parallel surfaces of the bare electrodes is nonzero, due to tunneling. Hence, since the surface area S of the bare electrodes is infinite, the total current $I = \int_S \mathrm{d}x\,\mathrm{d}y\,[\hat{z}\cdot\mathbf{j}(x,y)]$ is infinite. Therefore, we are interested in the *extra* current δI which is due to the presence of the junction, and is given by

$$\delta I = \int \mathrm{d}x\,\mathrm{d}y\ \left(\hat{z}\cdot[\mathbf{j}(\mathbf{r}) - \mathbf{j}^0(\mathbf{r})]\right) . \tag{2.33}$$

2.4 Time-dependent methods

2.4.1 Time-dependent density functional theory

In this dissertation, we will explore an approach to studying electron transport which is an alternative to the scattering formalism. One of the strengths of the approach we will describe is that it is inherently a time-dependent method, allowing us to study dynamical effects. We will therefore find it useful to introduce time-dependent density functional theory (TDDFT). The validity of TDDFT can be justified following theorem due to van Leeuwen:

van Leeuwen theorem. *A time-dependent particle density $n(\mathbf{r},t)$ obtained from a given many-particle system can, under mild restrictions on the initial state, always be reproduced by an external potential $V'(\mathbf{r},t)$ in a many-particle system with different many-particle interactions. Given the initial state of this other many-particle system the potential $V'(\mathbf{r},t)$ is unique up to a purely time-dependent function.*

The proof of this statement is somewhat lengthy and so we refer the reader to the original paper [38]. The utility of the theorem to the present problem lies in setting the many-particle interactions of the second system to zero. In

that case, the Van Leeuwen theorem tells us that there exists a time-dependent potential $V_{\rm KS}(\mathbf{r},t)$ such that the time-dependent density $n(\mathbf{r},t)$ will coincide with the density of the true Coulomb-interacting electronic system.[10] In the position basis, our noninteracting system evolves according to the Schrödinger equation

$$\left\{-\frac{1}{2}\nabla^2 + V_{\rm KS}(\mathbf{r},t)\right\}\phi_i(\mathbf{r},\sigma,t) = i\frac{\partial}{\partial t}\phi_i(\mathbf{r},\sigma,t)\,. \tag{2.34}$$

Similarly to before, $V_{\rm KS}$ is decomposed as

$$V_{\rm KS} = V(\mathbf{r},t) + V_{\rm H}(\mathbf{r},t) + V_{\rm xc}(\mathbf{r},t)\,, \tag{2.35}$$

where $V(\mathbf{r},t)$ is an external potential, and $V_{\rm H}(\mathbf{r},t)$ is the Hartree potential. Typically, the effect of the finite speed of light is ignored, and so $V_{\rm H}(\mathbf{r},t)$ is defined as in the static case: $V_{\rm H}(\mathbf{r},t) = \int \mathrm{d}\mathbf{r}' n(\mathbf{r}',t)/|\mathbf{r}-\mathbf{r}'|$.

One approximation for the time-dependent exchange-correlation potential is to ignore the time-dependence, and use a static functional:

$$V_{\rm xc}(\mathbf{r},t) \approx V_{\rm xc}(\mathbf{r}) \tag{2.36}$$

Using a static functional for the time-dependent problem in this way is called the adiabatic approximation. In particular, using static LDA in a time-dependent problem is called the adiabatic local density approximation (ALDA) [40].

2.4.2 Time-dependent current density functional theory

While much work has been done in attempts to create accurate time-dependent TDDFT exchange-correlation functionals, approximate functionals of the density $n(\mathbf{r},t)$ can be shown to suffer from an important deficiency [25, 41, 42]: a frequency-dependent local density approximation to $V_{\rm xc}[n(\mathbf{r},t)]$ does not exist. That is, TDDFT is correct if one knows the exact exchange-correlation functional, but

[10] TDDFT was first justified via the Runge-Gross theorem [39], which is a special case of the van Leeuwen theorem, and specifies that two densities which evolve as a result of two time-dependent local potentials must necessarily be different, provided that the local potentials differ by more than a purely time-dependent function.

if one does not know the exact functional, then any approximate functional will be incorrect. (For an example regarding a uniform electron gas responding to a small sinusoidal potential, see Appendix B.) Note that, in many cases, the correction to the approximate functional may be small [25, 43], but they remain nonzero unless the problem is truly static.

This so-called "ultra-nonlocality problem" motivates the development of time-dependent current density functional theory (TCDFT) [42]. In this construction, rather than using the density $n(\mathbf{r},t)$ as the central variable, one uses the current density $\mathbf{j}(\mathbf{r},t)$, which is the expectation value of the current density operator:

$$\hat{\mathbf{j}}(\mathbf{r},t) = \frac{1}{2}\sum_i \left[\hat{\mathbf{p}}_i \delta(\mathbf{r}-\hat{\mathbf{r}}_i) + \delta(\mathbf{r}-\hat{\mathbf{r}}_i)\hat{\mathbf{p}}_i\right] \tag{2.37}$$

Clearly, given an initial density $n(\mathbf{r},0)$ and a time-dependent current density $\mathbf{j}(\mathbf{r},t)$, one can in principle recover the time-dependent density via the continuity equation $\partial n(\mathbf{r},t)/\partial t = -\nabla\cdot\mathbf{j}(\mathbf{r},t)$.

Analogously to the way one can construct $V_{\rm xc}$ from the density n, the current density $\mathbf{j}$ can be used to construct an exchange-correlation vector potential $\mathbf{A}_{\rm xc}[\mathbf{j}]$. In the position basis, and in the absence of an externally-applied vector potential, the Hamiltonian takes the form

$$H = \frac{1}{2}\left(\frac{1}{i}\nabla + \frac{1}{c}\mathbf{A}_{\rm xc}(\mathbf{r})\right)^2 + V(\mathbf{r}) + V_{\rm H}(\mathbf{r}) + V_{\rm xc}(\mathbf{r})\,. \tag{2.38}$$

Similarly to the LDA in density functional theory, one can derive an exchange-correlation vector potential for the case of a weakly perturbed homogeneous electron liquid of uniform density [25, 42, 44]. The result is

$$\frac{1}{c}\frac{\partial A_{{\rm xc},i}(\mathbf{r},t)}{\partial t} = \frac{1}{n(\mathbf{r},t)}\sum_j \frac{\partial \sigma_{{\rm xc},ij}(\mathbf{r},t)}{\partial r_j} \tag{2.39}$$

where

$$\sigma_{{\rm xc},ij}(\mathbf{r},t) = \int_{-\infty}^{t} {\rm d}t \left\{\eta\left[\frac{\partial v_i}{\partial r_j} + \frac{\partial v_j}{\partial r_i} - \frac{2}{3}\nabla\cdot\mathbf{v}\delta_{ij}\right] + \zeta\nabla\cdot\mathbf{v}\delta_{ij}\right\}\,, \tag{2.40}$$

and i and j denote the Cartesian components of the position $\mathbf{r}$ and the velocity $\mathbf{v}$. The velocity is defined from the current density $\mathbf{j}$ and the density n via $\mathbf{v}\equiv\mathbf{j}/n$.

The coefficients η and ζ take the form of viscosities, and are in general time-dependent. Nifosi *et al.* [45] have made a numerical study using the Random Phase Approximation (RPA) [25] in order to calculate approximate values for η and ζ in the long wavelength limit, where the product of the characteristic wavelength of a perturbing external field q and the Fermi velocity $v_{\rm f}$ are much less than the frequency of the perturbing field ω. Conti *et al.* [46] have estimated typical values of η as a function of the instantaneous value of the density by parameterizing the results of Nifosi *et al.*; the formula itself is given in Appendix C.

The central feature of equation 2.40 that will be relevant for this dissertation is that the tensor $\sigma_{\rm xc}$ results in a hydrodynamic viscous force on the electrons. In Chapter 5, we will discuss the onset of turbulence in nanoscale systems, and argue that this viscous term is not enough to prevent the formation of turbulent eddies.

2.4.3 The propagator

Regardless of the form of the Hamiltonian $\hat{H}$, in any time-dependent formalism, one seeks to treat the Schrödinger equation

$$\hat{H}|\psi\rangle = i\frac{\partial}{\partial t}|\psi\rangle\,. \tag{2.41}$$

The solution to the Schrödinger equation can be written as

$$\psi(t) = \hat{T}\exp\left(-\mathrm{i}\int_0^t \mathrm{d}t'\hat{H}(t')\right)\psi(0)\,, \tag{2.42}$$

where we have used the time-ordering operator $\hat{T}$. This notation is defined as follows:

$$\begin{aligned}\hat{T}\exp\left(-\mathrm{i}\int_0^t \mathrm{d}t'\hat{H}(t')\right) \equiv \lim_{\Delta t\to 0}\Bigg\{&\exp\left(-\mathrm{i}\Delta t\hat{H}((N-1)\Delta t)\right)\\ &\times\exp\left(-\mathrm{i}\Delta t\hat{H}((\Delta t)\right)\times\ldots\times\exp\left(-\mathrm{i}\Delta t\hat{H}(0)\right)\Bigg\}\,,\end{aligned} \tag{2.43}$$

where $N = t/\Delta t$. That is, for each time $t_j \equiv j\Delta t$, we apply the operator $\mathrm{e}^{-\mathrm{i}\Delta t H(t_j)}$. The solution becomes exact in the limit that the timestep Δt goes to zero, although clearly for any numerical treatment, the timesteps will be small but finite.

Thus, implementing a solution to (2.42) numerically requires one to construct the matrix exponential $\mathrm{e}^{-\mathrm{i}\Delta t H}$, which is defined via the Taylor expansion

$$\mathrm{e}^{-\mathrm{i}\Delta t H(t)} \equiv \sum_{n=0}^{\infty} \frac{1}{n!}\big(-\mathrm{i}\Delta t H(t)\big)^n \,. \tag{2.44}$$

However, constructing the propagator directly from the Taylor expansion in this way is not ideal because the expansion is not numerically stable [47]. An improved method [48, 49] is to express the exponential equivalently in a series of Chebyshev polynomials Φ_n. The polynomials are only defined for arguments with less than unit magnitude, so $H(t)$ must be renormalized so that its eigenvalues range from -1 to 1; therefore, we define

$$H_{\mathrm{norm}} \equiv 2\frac{H - (\Delta E/2 + E_{\mathrm{min}})\hat{I}}{\Delta E} \,, \tag{2.45}$$

where E_{min} and E_{max} denote the minimum and maximum eigenvalues[11] of $H(t)$, and $\Delta E \equiv E_{\mathrm{max}} - E_{\mathrm{min}}$. With these definitions, we can write the expansion of the matrix exponential in terms of Chebyshev polynomials as

$$\mathrm{e}^{-\mathrm{i}\Delta t H(t)} = \mathrm{e}^{-\mathrm{i}(\Delta E/2 + E_{\mathrm{min}})\Delta t} \sum_{n=0}^{\infty} a_n \Phi_n\big(-\mathrm{i}\Delta t H_{\mathrm{norm}}(t)\big) \,. \tag{2.46}$$

If we define the action of a Chebyshev polynomial $\Phi_n(-\mathrm{i}H_{\mathrm{norm}})$ on a wavefunction $\psi(t)$ via $\phi_n \equiv \Phi_n(-\mathrm{i}H_{\mathrm{norm}})\psi(t)$, then we can generate the ϕ_n's via the recursion relation

$$\begin{cases} \phi_0 = \psi(t) \\ \phi_1 = -\mathrm{i}H_{\mathrm{norm}}\psi(t) \\ \phi_{n+1} = -2\mathrm{i}H_{\mathrm{norm}}\phi_n + \phi_{n-1} \,. \end{cases} \tag{2.47}$$

The coefficients a_n are given by

$$a_n(\alpha) = \int_{-\mathrm{i}}^{\mathrm{i}} \mathrm{d}x \frac{\mathrm{e}^{\mathrm{i}\alpha x}\Phi_n(x)}{(1-x^2)^{1/2}} = 2J_n(\alpha) \,, \tag{2.48}$$

where $\alpha = \Delta E \Delta t/2$, and $a_0 = J_0(\alpha)$.

[11] E_{min} and E_{max} can be given rigorous bounds by using the Gershgorin Circle theorem [50, 51]. For a second-order finite differencing approximation to the Laplacian with grid spacing Δx, this gives $E_{\mathrm{min}} = \min(V_{\mathrm{KS}}(\mathbf{r}))$, $E_{\mathrm{max}} = \max(V_{\mathrm{KS}}(\mathbf{r})) + 6/\Delta x^2$. For a fourth-order approximation to the Laplacian, we have $E_{\mathrm{min}} = \min(V_{\mathrm{KS}}(\mathbf{r})) - 1/4\Delta x^2$, $E_{\mathrm{max}} = \max(V_{\mathrm{KS}}(\mathbf{r})) + 31/4\Delta x^2$.

3

Approach to steady-state transport in nanoscale conductors

3.1 Introduction

The static scattering approach has been extensively used to treat steady-state transport in mesoscopic and nanoscopic conductors. The approach, as originally introduced by Landauer, treats the sample as a scatterer between two leads, which are connected adiabatically to two infinite electron reservoirs at different local electrochemical potentials [36, 52]. The reservoirs are just conceptual constructs which enable one to map the non-equilibrium transport problem onto a static scattering one [53, 54]. However, the ensuing steady state may not necessarily be the "true" steady state that is reached dynamically when a battery discharges across the sample. In addition, the static picture says nothing about the dynamical onset of steady states, their microscopic nature, or their dependence on initial conditions. These issues are particularly relevant in nanoscale structures where some of the assumptions of the static approach may hide important physical properties pertaining to the true charge dynamics.

In this Chapter we employ an alternative picture of transport in nanoscale systems in which we abandon the infinite reservoirs invoked by Landauer. Instead,

as recently suggested by Di Ventra and Todorov [13], we consider the current that flows during the discharge of two large but *finite* oppositely-charged electrodes connected by a nanojunction. Unlike the static, open boundary approach, the present approach permits one to describe the current within a microcanonical formalism where both energy and particle numbers are conserved quantities. In addition, due to the finite and isolated nature of the system, it can be demonstrated [13] that the *total* current flowing from one electrode to the other can be calculated *exactly* using time-dependent density-functional theory (TDDFT) [39] provided that one knows the exact functional, regardless of whether the system reaches a steady state or not.

We find that a quasi-steady state current, though lasting only for a limited period of time, can be established in the neighborhood of the nanojunction without any dissipation. This is simply due to the change in the spread of momentum of wavepackets as they move into a nanojunction and adapt to the given junction geometry. This effect occurs roughly in a time $\Delta t \sim \hbar/\Delta E$, where ΔE is the typical energy spacing of lateral modes in the junction. For a nanojunction of width w, $\Delta E \sim \pi^2\hbar^2/m_e w^2$ and $\Delta t \sim m_e w^2/\pi^2\hbar$. If $w = 1$ nm, Δt is of the order of 1 fs, i.e., orders of magnitude smaller than typical electron-electron or electron-phonon scattering times [55]. We indeed focus on the electron dynamics after the quasi-steady state has been established and make a connection between this dynamical picture and the Landauer's static approach. To this end, we consider a finite three-dimensional (3D) model gold nanojunction and a finite quasi-one-dimensional (1D) gold wire (see schematics in Fig. 3.1). These are the simplest structures for which the quantized conductance and current-voltage characteristics have been computed using the static scattering approach [56, 57] and have been measured experimentally for similar gold quantum point contacts [58]. Recently, Horsfield *et al.* have shown that a steady current is generated in a similar finite atomic chain [16]. Nevertheless the question of whether a steady state can be reached without including any electron-ion interactions remains unanswered in their work.[1] In addition to

[1] A.P. Horsfield and T. N. Todorov have communicated to us that they also find steady currents

answering this question, we show that one can define two local electron occupation functions on each side of the nanojunction. These are shifted in energy by an amount which can be interpreted, in the limit of large electrodes, as the "bias" of the corresponding open system. These functions depart from the equilibrium Fermi distributions by an amount which decreases with increasing electrode size. This verifies Landauer's hypothesis that "geometrical dilution" of wavefunctions is the most important aspect of a reservoir [59]. However, contrary to previous conclusions [60, 61]. we show that finite but long one-dimensional leads do not need to widen to constitute good "reservoirs", as long as one considers the electron dynamics in the junction before the electrons reach the edge of the system.

3.2 A simple demonstration using the tight-binding model

We now begin our study by using a simple time-dependent tight-binding (TB) model for noninteracting electrons where Coulomb interactions and correlation effects are absent. Later, we treat the problem using a fully self-consistent TDDFT approach in the adiabatic local density approximation (ALDA) [62].

Consider the N-site single-orbital TB Hamiltonian

$$H^{\mathrm{TB}} = \sum_{i=1}^{N} \epsilon_i |r_i\rangle\langle r_i| + \mathfrak{t} \sum_{i}^{N} |r_i\rangle\langle r_{i+1}| + \mathrm{H.c.}, \tag{3.1}$$

where there is one orbital state $|r_i\rangle$ per atomic site with energy ϵ_i and transfer matrix element $\mathfrak{t}$ connecting nearest-neighbor sites.[2] We then prepare the system such that half of the system has a deficiency of electrons, and the other half has a surplus. This can be done by increasing ϵ_i of the sites on one side of the system by an energy "barrier" E_B. For the 1D wire (see inset of Fig. 3.1), the interface

in the absence of inelastic effects but they have never reported their results in any publication (private communication).

[2]The matrix element $\mathfrak{t} = -11$ eV is chosen so that the time scales of the TB calculation are comparable to those in the TDDFT calculation for the same number of atoms in the system.

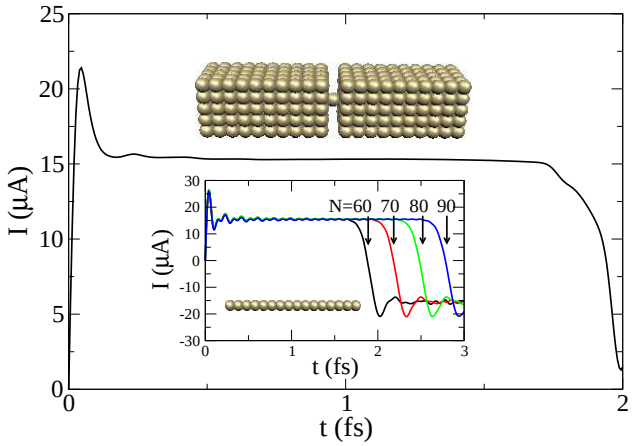

Figure 3.1 Current passing through the junction as a function of time for a 3D nanojunction (schematic is shown) calculated with a non-interacting TB model. Each of the electrodes consists of $5 \times 5 \times 30$ atoms arranged in a simple cubic geometry. The inset shows the corresponding current for a linear chain of N=60, 70, 80 and 90 gold atoms. In both cases E_B=0.2 eV (see text).

between the two regions separated by the barrier defines the nanoscale "junction". Taking this state as the initial state of the system, we then remove E_B, and let the electrons propagate according to the time-dependent Schrödinger equation (TDSE) with the time-independent Hamiltonian H^{TB}.[3]

Due to the closed and finite nature of the system, the total current can be calculated by time differentiating the charge accumulated on one side of the system, i.e.,

$$I(t) = -e\frac{d}{dt}\sum_{n=1}^{N/2}\sum_{i=1}^{N_L}\langle\psi^n(t)|r_i\rangle\langle r_i|\psi^n(t)\rangle. \tag{3.2}$$

Here $\psi^n(t)$ are the occupied single-electron states that are solution of the TDSE, and N_L is the number of sites on the left of the junction interface. Summation over spin degrees of freedom is implied.

The onset of a quasi-steady state for a 3D nanojunction is shown in Fig. 3.1,

[3]This is just one of the many (essentially infinite) initial conditions one can choose to initiate current flow. However, note that some initial conditions may not lead to a quasi-steady state. The question of the dependence of steady states on initial conditions has been addressed in Refs. [13] and [17], and will be analyzed in more detail in a future publication.

where we plot the current Eq. (3.2) as a function of time for $E_B = 0.2$ eV. In the inset, we show that a similar quasi-steady state current develops in 1D wires of different lengths, where the initial time energy barrier forces electrons to change the spread of electron momentum, and hence plays a role similar to that of the geometric constriction in the 3D case. In all cases, the current initially rises rapidly, but quickly settles in a quasi-constant value $I_{\rm ss}$.[4] In the 1D structures, small oscillations are observed which decay in time. The quasi-steady state lasts for a time t_d during which the electron waves propagate to the ends of the wire and back. The time t_d is a few femtoseconds for the considered cases, and can be made longer by increasing the length of the wires (see Fig. 3.1 inset). We have thus demonstrated numerically our initial conjecture: in a closed and finite nanoscale system, a quasi-steady state current with a finite lifetime can develop even in the *absence* of dissipative effects. The steady state is a direct consequence of the geometrical constriction experienced by the electron wavepackets as they propagate through the junction. This is in contrast with the conclusion of Ref. 17, where the establishment of a steady state is attributed to a "dephasing mechanism" of the electrons spreading in infinite electrodes.

In order to calculate the conductance of this closed system, we need to define a "bias". In this non-interacting electron problem, the energy barrier E_B seems a natural choice. However, that is not completely satisfying as it relates to the initial conditions and not to the electron dynamics. Let us instead define local occupation numbers for electrons in the left and right regions of the system. This concept is typically introduced as a starting point in the static approach to transport. Here we would like to define it dynamically. We then project the occupation for each eigenstate $|E_j\rangle$ of the Hamiltonian H^{TB}, i.e, $f(E_j,t) = \sum_n |\langle E_j|\psi^n(t)\rangle|^2$ onto the

[4]Note that, in the 3D case, a quasi-steady state can be established only if the typical energy spacing of lateral modes of the electrodes is much smaller than the corresponding one in the junction.

left- and right-hand side of the system,

$$\begin{aligned} f(E_j,t) &= \sum_n \Big| \sum_{i\le N/2} \langle E_j|r_i\rangle\langle r_i|\psi^n(t)\rangle \Big|^2 \\ &+ \sum_n \Big| \sum_{i> N/2} \langle E_j|r_i\rangle\langle r_i|\psi^n(t)\rangle \Big|^2 \\ &+ \sum_n 2\mathrm{Re}\Big\{ \sum_{i\le N/2} \langle E_j|r_i\rangle\langle r_i|\psi^n(t)\rangle \\ &\sum_{i> N/2} \langle \psi^n(t)|r_i\rangle\langle r_i|E_j\rangle \Big\}. \end{aligned} \tag{3.3}$$

We denote the first, second, and third term $f_L(E_j,t)$, $f_R(E_j,t)$, and $f_C(E_j,t)$, respectively. The quantity $f_C(E_j,t)$ is the sum of cross terms between the energy distribution on the left and on the right region. Note also that because the set $\{|E_j\rangle\}$ forms a complete orthonormal basis, $\sum_j f_L(E_j,t) = n_L$, $\sum_j f_R(E_j,t) = N - n_L$, and $\sum_j f_C(E_j,t) = 0$, where n_L is the total charge left to the junction at a given time. The quantities $f_L(E_j,t)$ and $f_R(E_j,t)$, normalized to two electrons per state, are plotted in Fig. 3.2 for two wires of $N = 100$ and $N = 500$ atoms immediately after the onset of the current.

One might naively think of these functions as broadened Fermi distributions centered at different "chemical potentials", separated by an energy $\Delta\mu$. A closer examination, however, reveals that they cannot be simply fitted to Fermi functions with just an effective thermal broadening. Instead, the very functional form of these non-equilibrium functions is different from a Fermi distribution. This is not surprising, as in this finite dynamical system electrons spread on each side of the junction and are not in any sort of local equilibrium in the electrodes. In addition, $\Delta\mu$ decreases with time because of the transport of electrons from one side of the system to the other. However, as long as we evaluate $f_L(E_j,t)$ and $f_R(E_j,t)$ at times much less than t_d, these functions approach two zero-temperature Fermi distribution functions centered at two different energies μ_L and μ_R, and $f_C(E_j,t)$ tends to zero for every E_j with increasing number of sites N in the electrodes. These energies can be interpreted as two local "chemical potentials" on the left

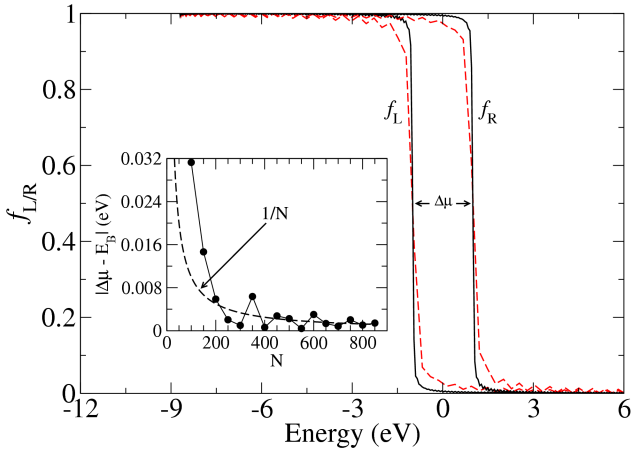

Figure 3.2 The local occupation functions $f_L(E_j, t)$ and $f_R(E_j, t)$ at a small time t after the onset of current for a linear chain of $N = 100$ (dashed line) and $N = 500$ (solid line) atoms. The inset shows the absolute difference between $\Delta\mu$ and initial energy barrier E_B as a function of N. The dashed curve is the function $1/N$.

and right side of the system, with $\Delta\mu = \mu_R - \mu_L$ approaching the initial energy barrier E_B with increasing N.

This asymptotic behavior as $N \to \infty$ is illustrated in Fig. 3.2 where $f_L(E_j, t)$ and $f_R(E_j, t)$ at a small t $(0 < t \ll t_d)$ are plotted for different values of N. The inset shows the absolute difference between $\Delta\mu$ and E_B as a function of N. The difference scales with N in the same way as does the separation of eigenstates of H^{TB} close to μ_L and μ_R. In three dimensions $N = N_x \times N_y \times N_z$, and it is then easy to prove, in this simple TB model, that $\Delta\mu$ approaches (albeit "nonvariationally") E_B as $\frac{1}{N_x} + \frac{1}{N_y} + \frac{1}{N_z}$ with increasing number of atoms in the three different directions (see inset of Fig. 3.2 for the 1D case). It is therefore evident that with increasing N, local equilibrium distributions can be effectively achieved in the two electrodes without inelastic effects: the electron waves moving into these regions are geometrically "diluted" in a practically infinite region of space and therefore do not "disturb" the local electron occupation. This is the equivalent of Landauer's definition of reservoirs [60]. Our results, however, show that this definition can be extended to one-dimensional electrodes as well. All this discussion allows us

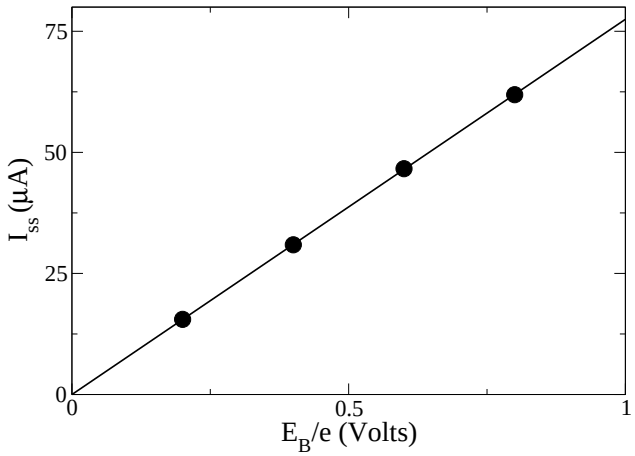

Figure 3.3 Current-voltage (I-V) characteristics at quasi-steady state of a finite 1D gold wire obtained using the TB approach. The corresponding conductance is 1.0 G_0. The TDDFT calculation yields a conductance of $0.99 \pm 0.03\ G_0$.

to define a conductance in this closed system in terms of the current at steady state I_{ss} and the value of $\Delta\mu/e$ for $N \to \infty$. The former converges very fast with increasing number of atoms, whereas the latter is the desired "bias" which, in turn, is simply the potential "barrier" E_B/e at $t = 0$. The current I_{ss} as a function of E_B/e is plotted in Fig. 3.3(a). The corresponding differential conductance is about 1.0 G_0 ($G_0 = 2e^2/h$) at all voltages, in good agreement with values obtained from the static approach [56, 57] and experimental observations for similar systems [58].

3.3 A density functional treatment of the linear chain

Finally, we study the onset of quasi-steady states in the presence of electron interactions that we describe at the mean-field level. We illustrate this point using TDDFT within the ALDA[5] for 1D wires. The corresponding current is plotted in

[5]The calculations reported here have been done using the `socorro` package (http://dft.sandia.gov/Socorro/mainpage.html), adapted by Ryan Hatcher to perform time-dependent calculations.

Fig. 3.4 for different lengths of a finite chain of gold atoms kept at a fixed distance of 2.8Å apart.[6] The lifetime of the quasi-steady state is short due to the limited system size but clearly increases with increasing length of the wire. What is more interesting, however, is the time for the quasi-steady state to set in. The initial transient time is found to be less than 1 fs, consistent with our original estimate.

The single-particle Kohn-Sham states [2, 39] have no explicit physical meaning so that the interpretation of the corresponding functions in Eq. (3.3) is less clear. On the other hand, the charge density, and thus, the electrostatic potential, are well defined quantities. We therefore define the conductance in this closed system in terms of the electrostatic potential drop between two points inside each electrode [13]. As in the case of $\Delta\mu$, the potential drop converges to the $t = 0$ value (plotted in the inset of Fig. 3.4) with increasing number of atoms.[7] The corresponding differential conductance is about $0.99 \pm 0.03\ G_0$, where the average value has been determined from the current in the wire with $N = 60$ atoms at t =1 fs.[8] It is worth pointing out that when the hopping parameter in the tight-binding calculation is chosen to match the dropoff time t_d in the TDDFT calculation for the same number of atoms, the initial transient time during which the quasi-steady state establishes itself in the tight-binding calculation is also less than 1 fs. This observation reinforces the notion that the geometric constriction effect is present irrespective of the inclusion of mean-field interactions.

In conclusion, we have shown numerically that a quasi-steady state can be

[6] As in the TB case, we construct the initial state of the system such that the left-hand side of the gold chain has a deficiency of charge, and the right-hand side has a surplus; we use a step-like potential to create this imbalance at $t = 0$. The current is similarly determined by differentiating in time the charge accumulating on the left side.

[7] Note that in the static formulation of transport there is a conceptual (albeit numerically small, see e.g. Di Ventra, M.; Lang, N. D. *Phys. Rev. B* **2002**, *65*, 045402) distinction between the chemical potential difference and the electrostatic potential drop, the conductance being usually defined in terms of the former.

[8] We have recently shown that there exist dynamical corrections to the electron conductance obtained using the ALDA which survive even in the limit of zero frequency [43]. These corrections depend on the gradient of the electron density and are therefore negligible for a gold quantum point contact. Combined with the theorem in Ref. 13 on the exact value of the TDDFT total current in a closed and finite system, this result shows that the TDDFT-ALDA current of a gold junction at steady state is very close to the exact many-body value.

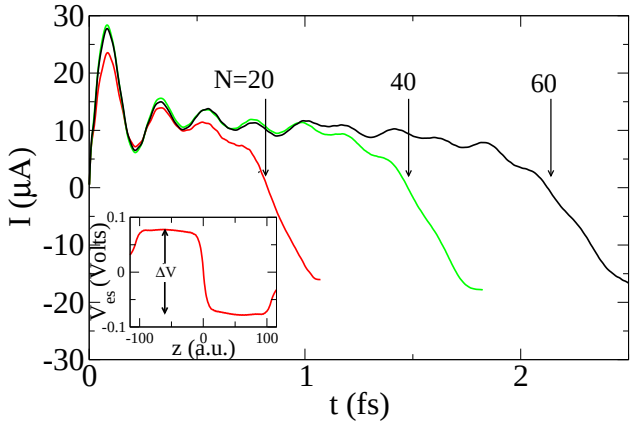

Figure 3.4 Current in the middle of the junction as a function of time for a linear chain of N= 20, 40, 60 atoms calculated using TDDFT-ALDA. The inset shows the electrostatic potential drop along the wire at $t = 0$ for a wire of 40 atoms.

achieved in a nanoscale system without dissipative effects, simply owing to the geometrical constriction experienced by electron wavepackets as they approach the nanojunction. We have also provided a practical scheme for dynamical conductance calculations in finite nanoscale systems that sheds new light on the assumptions of the standard static approach to steady-state conduction. The approach is also suited to study relatively unexplored effects such as transient phenomena, time-dependent charge disturbances, uniqueness of steady states and their dependence on initial conditions.

ACKNOWLEDGEMENTS

We thank Ryan Hatcher for providing help with the time-dependent calculations. We acknowledge financial support from the Department of Energy (DE-FG02-05ER46204).

Chapter 3 is a reprint of the material as it appears in Neil Bushong, Na Sai and Massimiliano Di Ventra, "Approach to steady-state transport in nanoscale conductors," *Nano Letters* **5**, 2569 (2005). Copyright 2007 by the American Chemical Society. The dissertation author was the primary investigator of this paper.

4

Microscopic Current Dynamics in Nanoscale Junctions

4.1 Introduction

Recent experimental progress has enabled imaging of coherent current flow dynamics in quantum point contacts formed in semiconductor heterostructures [63–66]. These advances in experimental techniques open the possibility that current flow through atomic or molecular junctions will be eventually imaged and controlled. Understanding the microscopic electronic flow patterns can aid the design of novel electronic devices. However, very few theoretical studies of current dynamics in nanoscale systems are currently available. Indeed, among the recent theoretical studies of transport in nanoscale systems, much emphasis has been placed on the steady-state conduction properties [3–12], whereas the transient behavior of the current remains an unexplored area.

Electronic transport in nanoscale junctions is usually formulated within the stationary scattering picture, such as the one due to Landauer [36], in which the conduction is treated as a collection of scattering events. This stationary approach, widely used to study transport in mesoscopic and nanoscale systems, has led to considerable success in understanding current-related effects other than the

conductance, including noise, inelastic effects and current-induced forces etc [67–74]. It has assisted our understanding of the microscopic current distribution as well [75, 76]. Nevertheless, the stationary approach assumes that the system is in a steady state, leaving the questions of how a steady current establishes itself and what other phenomena are related to the dynamical formation of steady states in a nanojunction unsolved.

The dynamical nature of the current flow is better addressed in a time-dependent approach than in the stationary one. Time-dependent or AC transport approaches have been previously introduced in mesoscopic conducting systems [77–79]. Recently, an increasing amount of effort has been directed toward developing ab-initio time-dependent approaches for nanoscale systems [13–22, 80]. One such method was developed to study the AC conductance using the time-dependent density functional theory [39] (TDDFT) combined with absorbing boundary conditions [14]. This method, however, is affected by the arbitrariness of how and where the absorbing potentials are added, while the effect of the absorbing potential on the conduction in nanojunctions is unclear. Other methods have been developed based on the Landauer scattering formalism of transport that employ open boundary conditions [15, 17–19].

More recently, a microcanonical formalism that treats electronic transport as a discharge across a nanocontact connecting two large but finite charged electrodes was introduced [13]. (We provided a demonstration of this method in Chapter 3.) The formulation employs TDDFT to study the dynamical formation of quasi-steady currents, local chemical potentials [80], and electron-ion interactions [16]. This formalism would yield the exact total current flowing from one electrode to the other if the exact functional were known, regardless of whether the system achieves a steady state. In practice, in ab-initio transport caculations, one only uses approximate forms of the functional such as the adiabatic local density approximation (ALDA). It has been shown recently that the electronic correlation effect beyond the ALDA gives rise to additional resistance in molecular junctions [43, 81–83]. The spurious self-interaction implicit in the ALDA further complicates calcula-

tions of the conduction properties [84–86]. The sensitivity of various transport properties to the suggested corrections remains only partially understood.

The dynamical establishment of a quasi-steady current has been investigated by a number of authors [16, 17, 80]. It has been demonstrated that a quasi-steady current can establish itself across a junction on a femtosecond time scale without the presence of inelastic scattering [80]. This is due to the geometrical "squeezing" experienced by the electrons crossing the nanojunction [13]. The conductance calculated from the microcanonical formula was shown to be in good agreement with that obtained from the static DFT approach in prototypical atomic junctions [16, 80] as well as in molecular junctions [87]. Nevertheless, a study of the microscopic behavior of the electron flow, and in particular of the current flow morphology in nanojunctions, is still lacking.

In this chapter, we carry out real-time numerical simulations of current flow in metallic nanojunctions using the microcanonical formalism, where we employ TDDFT within the ALDA, using a quasi-2D system geometry. We restrict the forthcoming discussion to the dynamical behavior of electron/hole charges in the nanojunctions under the linear response regime, i.e., in which the bias is weak and the current-voltage characteristics are linear. The chapter is organized as follows. In Sec.4.2 we discuss model transport systems and numerical methods. In Sec.4.3, we present and discuss simulation of current dynamics in jellium and atomic junctions. We also analyze the effects of hydrodynamic pressure and electrode surface charges on the dynamics of the flow. In Sec.4.4, we summarize the main conclusions of our work.

4.2 Model and Methods

The nanoscale junction geometry studied in this chapter is illustrated in Fig. 4.1. A narrow constriction separates two large but finite electrodes. We begin the simulations by applying a step function-like electric bias across the junction such that the two electrodes bear equal and opposite potentials offset relative to the poten-

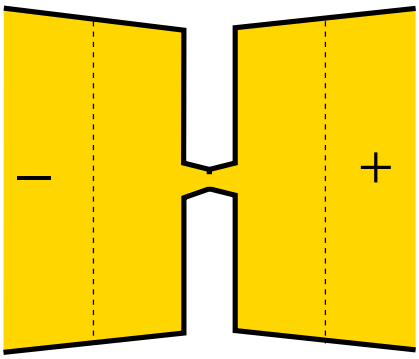

Figure 4.1 Sketch of the nanojunction geometry that is studied in the chapter. At $t < 0$, a bias in the form of $V(z) = V_0[\mathrm{H}(z - z_a) - \mathrm{H}(-z - z_a)]$ is applied to the junction (the central constriction is at $z = 0$) such that the regions $|z| > z_a$ bear a potential offset from the central constriction, where $H(z)$ is the Heaviside step function.

tial at the center of the junction. The distance from where the discontinuity of the bias happens to the center of the junction is z_a (see Fig.4.1). This bias induces a charge imbalance between the two sides of the system. At $t = 0$, we remove the bias and a discharge through the nanojunction ensues. The Kohn-Sham initial state therefore corresponds to the ground state of the Hamiltonian in the presence of the bias. Here, we are interested in the transient behavior during the phase in which the current is in the process of establishing a quasi-steady state and immediately thereafter, i.e., long before the electrons that have passed through the constriction have had chance to reach the far boundary of the electrodes.

To separate the effects of the electrons and of the atomic lattice, we have carried out calculations using a jellium model and an atomic model. In the jellium calculations, the electrodes are represented by two large jellium slabs 2.8 Å thick. The contact is a rectangular jellium block 2.8 Å wide and as thick as the electrodes. The distance between the jellium electrodes is 9.8 Å. In the atomic calculations, the junction is represented by two planar arrays of gold atoms sandwiching a single gold atom. We employ TDDFT and solve the effective single-particle Schrödinger

equation

$$i\hbar\dot{\psi}(\mathbf{r},t) = \left[-\frac{\hbar^2\nabla^2}{2m} + V_{\text{eff}}(\mathbf{r},t)\right]\psi(\mathbf{r},t), \tag{4.1}$$

where the effective potential is given by

$$V_{\text{eff}}(\mathbf{r},t) = V_{\text{ext}}(\mathbf{r},t) + \int \frac{\rho(\mathbf{r},t)}{\mathbf{r}-\mathbf{r}'}d\mathbf{r}' + V_{\text{xc}}(\mathbf{r},t). \tag{4.2}$$

The term $V_{\text{xc}}(\mathbf{r},t)$ is the exchange-correlation potential calculated within the adiabatic local-density approximation. The external (ionic) potential is modeled using pseudopotentials for the atomic calculations [88], while in the jellium model it is a local operator related to the uniform positive background jellium density ρ_0 via $V_{\text{ext}}(\mathbf{r}) = \int \frac{\rho_0}{\mathbf{r}-\mathbf{r}'}d\mathbf{r}'$, where ρ_0 equals to $(\frac{4\pi r_s^3}{3})^{-1}$ inside the jellium and zero outside, and r_s the Wigner-Seitz radius. In the jellium model, we choose $r_s = 3a_B$ (a_B = Bohr radius) which gives a good representation of bulk gold (see also discussion below). A "free-space" boundary condition is implemented such that the long-range potential is constructed only from the densities in the supercell [89]; that is, the system is not periodic. Additional numerical details can be found in Appendix 4.5. The single-particle time-dependent current density is calculated via

$$\mathbf{j}(\mathbf{r},t) = \sum_n \frac{\hbar}{2mi}\left[\psi_n^*(\mathbf{r},t)\nabla\psi_n(\mathbf{r},t) - \nabla\psi_n^*(\mathbf{r},t)\psi_n(\mathbf{r},t)\right], \tag{4.3}$$

where ψ_n denotes individual Kohn-Sham single-particle states.

Even if the contact between the electrodes were removed, the current between the two electrodes would not completely vanish because of quantum tunneling. This bare tunneling current can conveniently be used to compare the jellium and the atomic calculations. The jellium edges are placed at half the interplanar spacing of the lattice [90]. This way, the jellium model and the pseudopotential calculations both yield tunneling current densities of ~ 0.05 μA/Å^2 at a bias of 0.2V. The agreement indicates that the jellium model is a good representation of two large metal electrodes. This is consistent with the results of previous density-functional calculations [91].

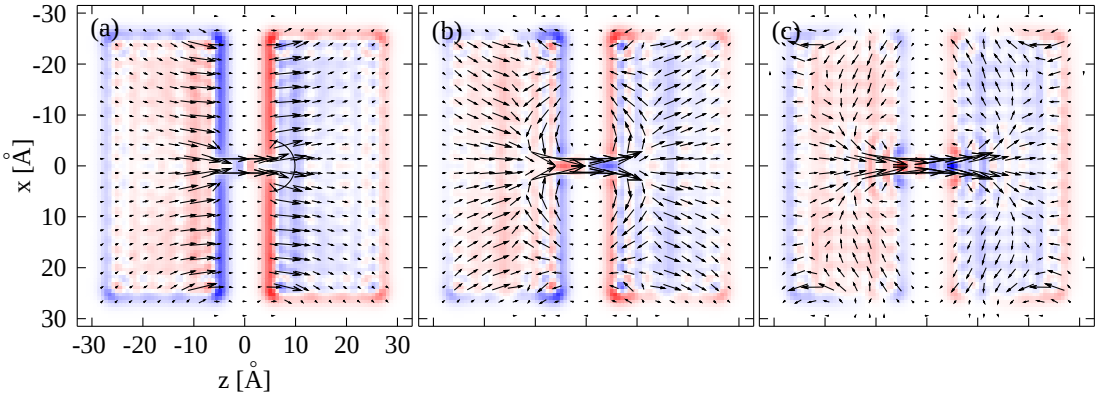

Figure 4.2 Current flux for a series of times in a nanoscale quantum point contact system in the jellium model. The applied bias at $t < 0$ is $\Delta V = 0.2$ V. The field lines in each panel depict the direction and amplitude of the current density vectors, while the colors give extra electron (red) or hole (blue) density. (a) $t = 0.4$ fs ; (b) $t = 0.8$ fs ; (c) $t = 1.6$ fs. In (a), the semicircle marks the contour along which the radial component of the current density is calculated (see text and Fig. 4.3).

4.3 Results and Discussion

4.3.1 Flow dynamics through jellium modeled junctions

In a nanojunction such as an atomic point contact, the dimensions of the leads are usually much larger than those of the central constriction. In addition, not far from the contact, we expect the electron momentum to converge to the value characteristic of the bulk leads. Therefore, the momentum of an electron coming from the leads and entering the contact has to change considerably. This gives rise to resistance, and for a truly nanoscale junction, this momentum mismatch is mainly responsible for the establishment of quasi-steady states [13, 80]. Using the above dynamical approach we can now study how this translates into microscopic current flow through the nanocontact and into the leads by calculating the current density at different times.

To begin, we follow the method described in the preceding section to impose a charge imbalance in the jellium model system. A discussion of the effect of the

lattice on the flow dynamics will be presented in the following section. The initial bias is chosen such that the discontinuity happens at the edge of the jellium slab near the central constriction (i.e., $z_a \cong 5$ Å). The flow pattern is independent of the location of the discontinuity once the current starts to flow through the center of the junction. In Fig. 4.2, we plot three snapshots of the current density to illustrate the evolution of the flow. Due to the bias offset near the jellium edges, a dipolar layer forms on each of the two contact-electrode interfaces. As a result, the initial current flow is uniform on both sides as shown in Fig. 4.2(a). Very little current flows in the nanojunction at this point, however the current steadily rises. In Fig. 4.2(b), the current density becomes convergent toward the center of the nanojunction. Interestingly, as the excess charge from the left electrode reaches the contact, there is a period of adjustment during which the dominant flow is in the lateral direction, i.e., parallel to the facing surfaces of the electrodes.

To quantify the evolution of the angular distribution of the electron flow, in Fig. 4.3 we plot a time series of the radial component of the current density along a semicircle contour centered on the junction as a function of the angle on the semicircle (see Fig. 4.2(a)). One can see that initially a "wave" of excess charge approaches the nanocontact. Then, the radial current density peaks at very large angles ($\sim \pm 75°$); i.e., the current density near the contact is dominated by the flow along the electrode edges in the lateral direction. The peaks then gradually move towards the central axis, and the current density adjusts to a more "focused" pattern as shown in Fig. 4.2(c). Besides the junction in the plot, we also examined a junction consisting of a jellium circular "island" between the electrodes. There we also observed edge flow. The edge flow is not a quantum interference pattern, and cannot be compared with the fringes observed in the 2D electron gas quantum point contacts [66]. Instead, we suggest that the flow pattern is controlled by hydrodynamic effects and forces due to surface charges. We analyze these in Sec. 4.3.3.

The structure of the current density is analogous to a classical fluid flowing across a narrow constriction. This is not surprising because an inhomogeneous

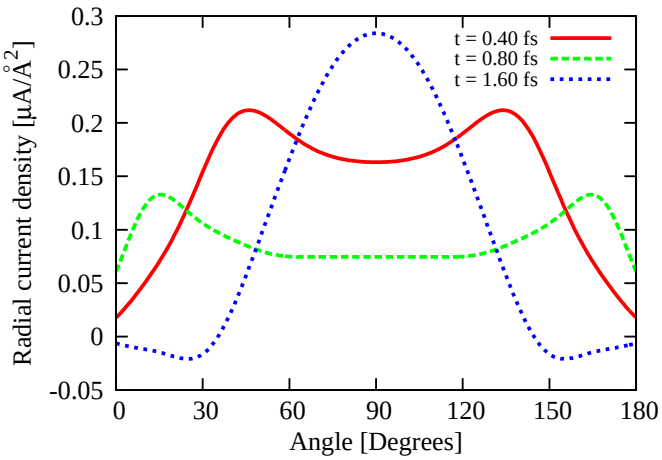

Figure 4.3 Time series of the radial amplitude of the current densities along a semicircle of radius 3Å centered on the nanojunction, as a function of angle along the contour.

electron system can be indeed characterized by a set of hydrodynamical relations expressed in terms of the particle density and velocity field of the electron liquid [92–95]. More recently, in particular, a hydrodynamical approach was proposed for nanoscale transport systems [95], further strengthening a resemblance between the electron liquid and a classical liquid. We note that the present calculations do not take into account the physical viscosity of the electron liquid[1] [46]. An inviscid fluid can therefore be used as a model for the dynamical behavior of the present electron liquid.

4.3.2 Flow dynamics through atomic junctions

The jellium model was a convenient way to probe the microscopic current dynamics in an electron gas. To understand the influence of the lattice on the flow, we carried out simulations that included an ionic background modeled by pseudopotentials. The atomic calculations were carried out for gold nanojunctions

[1]Note that in practical calculations, the electron liquid can have a nonvanishing numerical viscosity due to the discrete grid spacing.

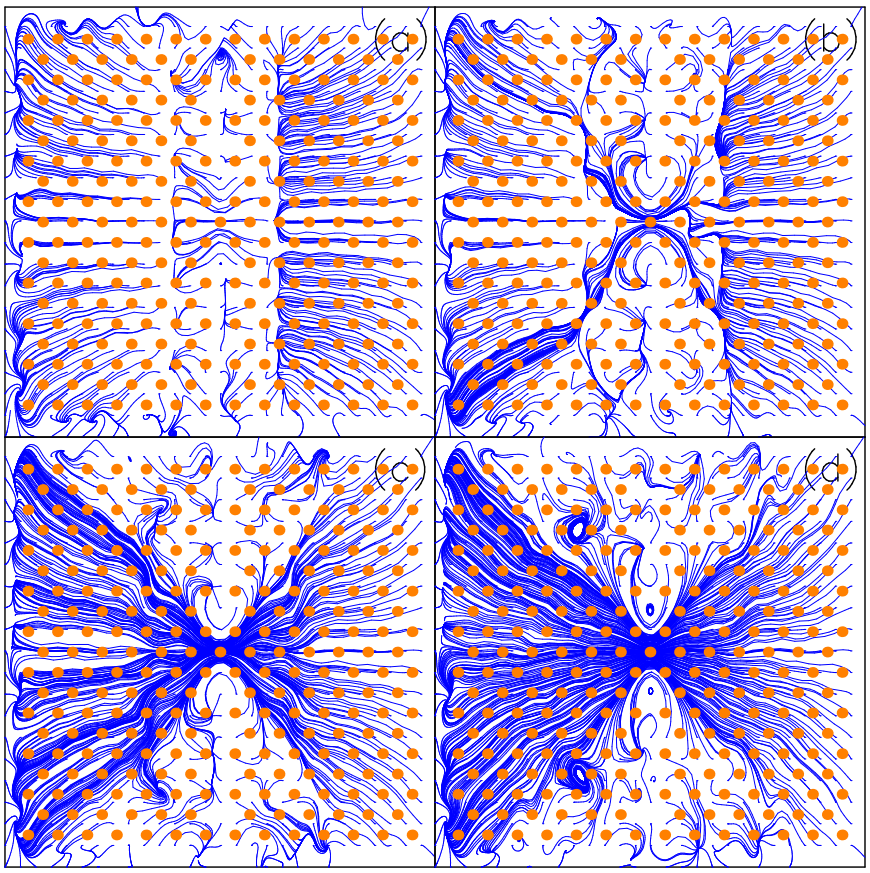

Figure 4.4 Time sequence of electron current streamlines in the atomic junction described in Sec.4.2. Panels (a) - (d) correspond to $t = 0.2$, 0.25, 0.3, and 0.35 fs, respectively. The dots denote atomic sites that corresponds to the (001) facets of the gold FCC lattice. The applied bias at $t < 0$ is $\Delta V = 0.2V$. The current density field is symmetric under the transformation ($z \to -z$ and $j_x \to -j_x$); slight asymmetries in the figure are an artifact of the plotting algorithm.

and were initialized in the same way as the jellium calculations. The theoretical and experimental conductance are in very good agreement for this system [58]. We chose lattice arrangement that corresponds to the (001) and (111) facets of the gold FCC lattice.

Electric current streamlines at different times in the simulation are plotted in Fig. 4.4(a) - (d). The streamlines are calculated by integrating the current density field upstream and downstream, $d\mathbf{r}/ds = \pm\mathbf{j}(\mathbf{r}(s))$. The morphology of the current flow in the atomic junction and in the jellium model is remarkably similar,[2] indicating that the jellium model is a good representation of the gold electrodes. Nevertheless, a number of new features appear in the atomic calculations.

Fig. 4.4(c) shows that once a steady flow through the junction is established, the current spreads into a wedge-shaped region inside the electrodes. The flow morphology for each of the two different lattice arrangements is similar except that the flow spreads over a broader wedge-shaped region in the (111) lattice. Another common feature in the atomic calculations is the presence of a stagnant zone at the corner of the electrode boundary. There is little current flow into or out of this zone. This is similar to a classical fluid where a stagnant zone can sometimes be located at the entrance or exit of a channel.

One profound difference between the atomic and the jellium calculations is the formation of eddies evident in the former but not in the latter. In the jellium calculations carried out within the linear-response bias regime, the current flux lines are laminar. In contrast, in the atomic calculations, the eddies appear as localized circular flow that can be observed in Fig. 4.4(d). The eddies develop in both electrodes and the size of the eddies is comparable to the interatomic distance. The eddies are reminiscent of the vortices that form in a classical fluid at higher Reynolds number when the fluid encounters obstacles. As is well known, vortices can also occur when velocity shear is present within a continuous fluid

[2]The nonuniformity of the density of stream lines is partially due to the fact that we have calculated the streamlines using random initial points. The lines becomes denser when two or more initial points belong to nearby streamlines.

(Kelvin-Helmholtz instability). We suggest that the lattice ionic obstacles and the boundaries separating the flow zone and the stagnant zone facilitate the formation of the observed eddies in our simulations.

The formation of current vortices has been previously reported in 2D ballistic quantum billiards [96, 97]. In these quantum systems, a rich variety of flow patterns ranging from regular to chaotic is possible. While we cannot draw direct analogies with these open and mesoscopic transport systems, we can speculate that an unstable and turbulent flow [98] can also develop in nanotransport systems. We have argued that the ALDA electron liquid in our simulations corresponds approximately to an inviscid fluid. We therefore suggest that in the presence of a lattice, hydrodynamical instabilities, or turbulence can occur in nanotransport systems even in the absence of a physical viscosity. For further discussion of electron turbulence in nanoscopic systems, see Chapter 5.

4.3.3 Hydrodynamics and the formation of surface charges

To understand what drives the edge flow along the electrode surfaces, we examine the evolution of the charge distribution near the surfaces. For this purpose, we apply a step-function bias such that the potential discontinuity in each electrode occurs at $z_a \cong 10$Å, which cuts across the electrode, as illustrated in Fig. 4.1. In Fig. 4.5(a), we plot a time series of the $x-y$ plane-averaged excess charge density along the z axis. At $t = 0$, two symmetric dipolar layers form inside the electrodes as a result of the bias offsets. As the current starts to flow through the contact and gradually reaches a quasi-steady state, a global charge redistribution becomes apparent. The dipolar layers gradually vanish and are replaced by surface charge layers that form at the contact-electrode interfaces. The charge contour plots Fig. 4.5(b-c) further illustrate the formation of surface charges as a result of current flow.

The formation of surface charges around the central constriction is reminiscent of the formation of residual-resistivity dipoles introduced by Landauer [36]. It has

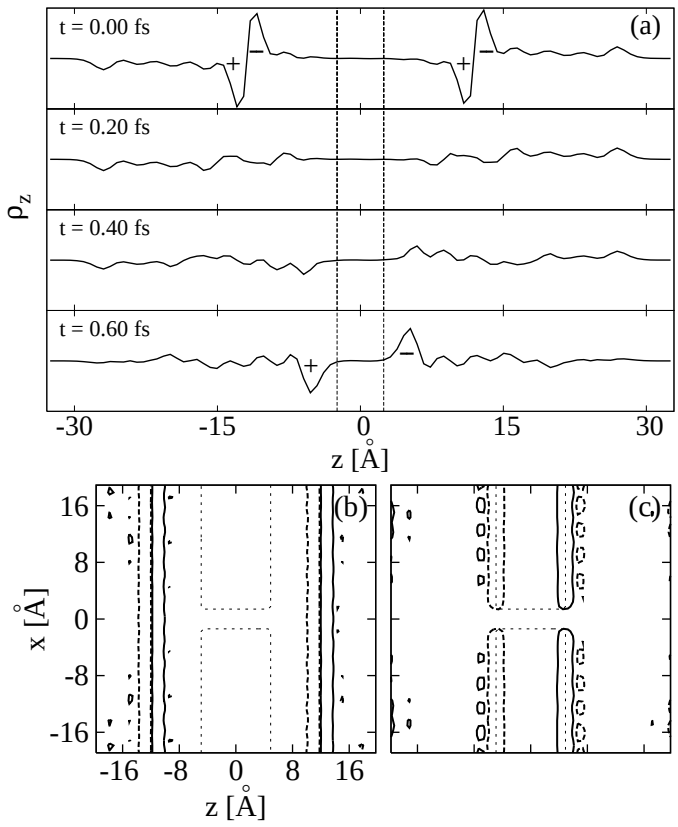

Figure 4.5 (a) Planar averaged charge density from $t = 0$ to $t = 0.6$ fs. The change in the peaks indicates the dynamic process in which excess charge builds up at the surfaces. The sign of the surface charges indicates that electron charges accumulates on the right and hole charges on the left. (b) - (c) Excess charge in the vicinity of the contact at $t = 0$ and $t = 0.6$ fs. Thick solid lines indicate excess electrons, while thick dashed lines indicate excess holes. Thin dashed lines mark the edges of the jellium electrodes and the contact.

been suggested that a continuous current flow arriving at a junction must be accompanied by self-consistently formed charges at the electrode surfaces [91]. The effect should be taken into account to correctly characterize the electrostatic potential and the nonequilibrium conducting properties in a transport calculation [99]. In this chapter we provide the first numerical demonstration of the dynamical formation of the surface charges in a time-dependent calculation.

We have already observed that, as the surfaces of the electrodes are populated by excess charges, a lateral flow starts to develop along the surfaces. This behavior is illustrated in Fig. 4.3 where the radial current flux at $t = 0.8$ fs shows two pronounced peaks at very large angles. We attempt to interpret this behavior within the framework of an effective classic hydrodynamic model of an inviscid charged fluid. The acceleration of the fluid is then given by Euler's equation $\partial\mathbf{v}/\partial t + (\mathbf{v}\cdot\nabla)\mathbf{v} = -\nabla P/m_e n - \nabla\varphi/m_e$, where $\mathbf{v}$ is the fluid velocity, n is the fluid particle density, m_e is the electron mass, and φ is the electrostatic potential. The first term on the right hand side is the acceleration due to a gradient in electron pressure. The second term is the acceleration due to the electric field of the excess charges on the surfaces of the electrode. The electric field drives the electrons/holes toward the surfaces to cancel out the excess charges.

The inertial term in the above equation can be estimated as $|(\mathbf{v}\cdot\nabla)\mathbf{v}| \sim v^2/L \sim 10^6 m^2/s^2 \times L^{-1}$. Here, L denotes the characteristic length scale on which we expect a departure from ballistic flow, so that $\nabla \sim L^{-1}$. Velocity of the flow in the simulation reaches $v \sim 10^3 m/s \ll v_F$, where $v_F \approx 1.4 \times 10^6 m/s$ is the Fermi velocity of bulk gold. The hydrodynamical pressure can be calculated from derivative of the ground state energy $P/n = -\frac{r_s}{3}\epsilon'(r_s)$, where $\epsilon(r_s)$ is the energy per particle [25]. Therefore, $|\nabla P|/m_e n \sim \frac{1}{5}v_F^2|\nabla n|/n$. Here, we included only the ground state energy of a noninteracting electron gas, $\epsilon_0(r_s) = \frac{3}{5}\epsilon_F$.[3] Let δn denote the change of the particle density as a result of the current or the formation of the surface charges. For the atomic junction in Fig. 4.4, we find that typically

[3]Including the exchange and correlation effects reduces the pressure slightly compared to the noninteracting results.

$\delta n/n \lesssim 0.01$. Then, the acceleration due to the pressure gradient

$$\begin{aligned} |\mathbf{a_P}| &= \frac{|\nabla \mathbf{P}|}{m_e n} \sim \frac{1}{5}\frac{v_F^2}{L}\frac{\delta n}{n} \\ &\lesssim 3 \times 10^9 \frac{m^2}{s^2} \times L^{-1}. \end{aligned} \tag{4.4}$$

To estimate the magnitude of the electrostatic acceleration, we treat the layer of charge induced on the facing surfaces of the electrodes (as illustrated in Fig.4.5c) as an infinite uniformly charged wire. The electric field of the wire is given by $|\nabla\varphi| = \lambda/2\pi\varepsilon_0 L$, where λ is the linear density of excess charge, L is the distance to the wire, and ε_0 is the vacuum permittivity. The linear charge density is calculated by averaging the charge density difference $e\delta n$ between the configuration with and without the current flow over the layer in which the charge accumulated at the contact-electrode interfaces. For the same junction, we find $\lambda \sim 0.016\ e/\text{Å}$. The acceleration of charges due to this electric field can be calculated

$$\begin{aligned} |\mathbf{a_{el}}| &= \frac{e}{m_e}\frac{\lambda}{2\pi\varepsilon_0 L} \\ &\sim 5 \times 10^{11} \frac{m^2}{s^2} \times L^{-1}. \end{aligned} \tag{4.5}$$

These crude estimates imply that

$$|(\mathbf{v}\cdot\nabla)\mathbf{v}| < |\mathbf{a}_P| < |\mathbf{a}_{el}|, \tag{4.6}$$

which suggests that the hydrodynamic pressure gradients dominate over the inertia of the fluid (the flow is subsonic and compressible), while the peak electrostatic force due to the surface charges is comparable to or larger than the pressure gradient force before the surface charge has been passivated. Therefore, it is plausible that the lateral flow observed in the simulation is primarily of electrostatic origin. In different junction geometries or in a different conducance regime, the ordering in Eq. 4.6 may be different.

We have also carried out a similar simulation using a parabolically-shaped constriction that resembles a quantum point contact in the 2D electron gas. At a similar bias as in the non-parabolic junctions, we find similar surface charge accumulation along the boundaries of the electrodes in the vicinity of the contact. We believe the analysis we provided applies to this case as well. To the best of our knowledge, the accumulation of the surface charges has not been reported in adiabatic quantum point contacts before. It would thus be interesting to develop experimental techniques to explore the surface region of the quantum point contact in a 2D electron gas and the charge accumulation that we observe in our simulations.

4.4 Conclusions

In this chapter, we used jellium and pseudopotential methods to study the time-dependent current flow morphology and the charge distribution in discharging nanojunctions. We showed that the electron flow in the nanojunctions exhibits hydrodynamic features analogous to a classical fluid. We found that in the atomic case the current flow evolves into wedge-shaped pattern flanked by stagnant zones. The flow develops nonlaminar features including eddy currents. We suggest that the ionic lattice plays a role in the development of these features. We also demonstrated that excess surface charges accumulate dynamically along the electrode. In addition, we observed that for a period of time, there is strong current flow is in the transverse direction. We employ an order of magnetitude argument to suggest that this flow is driven by hydrodynamical forces due to the electron pressure and electrostatic force due to the surface charge distributions.

The present study, along with the previous study in Chapter 3 [80], demonstrate that the finite geometry approach combined with time-dependent density-functional theory can be used to probe the transient behavior of the current in nanojunctions such as atomic-scale point contacts. The present approach supplements existing methods that are based on the static scattering picture and provides

another tool to studying nanoscale transport phenomena from first principles.

The flow patterns we observe in metallic nanojunctions can be generalized to a number of other systems, such as molecular junctions, although many details will vary. In view of the recent advances in microscopic imaging techniques of coherent current flow in quantum point contacts in a 2D electron gas [66], we hope that new experimental work exploring the behavior of current flow in atomic contacts and molecular junctions will soon emerge.

4.5 Numerical details

We performed time-dependent density-functional calculations using a standard program package `socorro` [88] and an in-house program which implements TDDFT within the jellium model. The gold ions were modeled by norm conserving Hamann pseudopotentials with $6s$ electrons as valence electrons [37]. We used the Perdew-Zunger (1981) LDA exchange-correlation functional [34]. The atomic calculation employed a plane-wave basis set, with an energy cutoff of 204 eV, which corresponds to grid spacing of 0.2Å. The energy eigenvalue varies by less than 1% by increasing the cutoff by 66%. In the jellium case, the calculations were performed using a real-space basis set where the space is uniformly discretized and the grid spacing is 0.7 Å. The eigenvalue varies less than 3% by decreasing the grid spacing by 66%. The time evolution operator is represented using the Chebyshev method [48], with a time step of 5×10^{-4} fs in the atomic case and 5×10^{-3} fs in the jellium case.

ACKNOWLEDGEMENTS

This work was supported by the Department of Energy Grant No. DE-FG02-05ER46204.

Chapter 4 is a reprint of the material as it appears in Na Sai, Neil Bushong, Ryan Hatcher and Massimiliano Di Ventra, "Microscopic current dynamics in nanoscale junctions," *Physical Review B* **75**, 115410 (2007). Copyright 2007 by the American Physical Society. The dissertation author was a co-author of this paper.

5

Electron turbulence at nanoscale junctions

5.1 Introduction

As mentioned in the previous Chapters, electron transport through a nanoscale junction is usually described as a scattering problem [3–7, 10, 36, 52, 100]. On the other hand, it has been shown [44, 92, 94, 95] that the behavior of the electron liquid obeys dynamical equations of motion which are similar in form to those governing the dynamics of classical liquids. In particular, it was recently shown [95] that the time-dependent Schrödinger equation (TDSE) for electrons flowing across a nanostructure can be cast in the form of generalized Navier-Stokes equations. A consequence of this analogy is the prediction that under certain conditions the laminar flow of the liquid may become unstable and turbulent behavior is expected [95, 98, 101]. One can then borrow knowledge from classical fluid dynamics and hypothesize that the electron flow will make a transition from laminar to turbulent regimes, if, e.g., the current is increased. As in a classical liquid, if, for instance, electrons flow from one electrode (call it the top electrode) to another (call it the bottom electrode) across a nanojunction, turbulence would first manifest itself with the break-up of the top-down symmetry of the electron flow [98, 101]. By

increasing the current further one should observe the formation of eddies in proximity to the junction. These turbulent eddies are created because of the larger kinetic energy in the direction of current flow (longitudinal kinetic energy) compared to the transverse direction (transverse kinetic energy). By increasing the current further, the disparity between longitudinal and transverse components of the kinetic energy increases, and the system flow eventually breaks any remaining symmetry, thus developing turbulence fully [98, 101]. Despite the prediction of turbulent behavior of the electron liquid in nanostructures [95] an explicit demonstration of this phenomenon and the analysis of its microscopic features has not been presented yet.

In this Chapter we set to show numerically turbulent effects for the electron liquid crossing a nanojunction both by solving directly the TDSE, and by solving the generalized Navier-Stokes equations derived in Ref. 95. These read

$$D_t n(\mathbf{r},t) = -n(\mathbf{r},t)\nabla\cdot\mathbf{u}(\mathbf{r},t)\,,$$
$$mn(\mathbf{r},t)D_t u_i(\mathbf{r},t) = -\partial_i P(\mathbf{r},t) + \partial_j \pi_{i,j} - n(\mathbf{r},t)\partial_i V_{\rm ext}(\mathbf{r},t)\,. \tag{5.1}$$

Here, n is the electron density, $\mathbf{u}=\mathbf{j}/n$ is the velocity field, i.e. the ratio between the current density $\mathbf{j}$ and the density, and $D_t = \frac{\partial}{\partial t} + \mathbf{u}\cdot\nabla$ is the convective derivative [98]. $P(\mathbf{r},t)$ is the pressure of the liquid, $V_{\rm ext}(\mathbf{r},t)$ an external potential, and $\pi_{i,j}$ is a traceless tensor that describes the shear effect on the liquid. It has the form

$$\pi_{i,j} = \eta\left(\partial_i u_j + \partial_j u_i - \frac{2}{3}\delta_{i,j}\partial_k u_k\right)\,, \tag{5.2}$$

where $\eta = \hbar n f(n)$ is the viscosity of the electron liquid and $f(n)$ is a smooth function of the density [46].

5.2 A density functional treatment using jellium

In analogy with the classical case we expect that the atomic structure, and in particular atomic defects in proximity to the junction, play the role of "obstacles" for the liquid and thus favor turbulence. Since we aim at showing that

turbulence develops irrespective of the underlying atomic structure, we consider electrons interacting with a uniform positive background charge (i.e., the "jellium" model [91]). The system we consider therefore consists of two large but finite jellium electrodes– subject to a bias– connected via a nanoscale jellium bridge. (The jellium edge of this system is represented with solid lines in each panel of Fig. 5.1.) We choose the density of the jellium at equilibrium typical of bulk gold ($r_s \approx 3a_0$). For computational convenience we choose a quasi-2D system, approximately 2.8 Å thick.[1] Note that, everything else being equal, a quasi-2D geometry *disfavors* turbulence compared to a 3D one. We thus expect that if turbulence develops in our chosen quasi-2D geometry with given thickness, then turbulence will develop even more easily if we leave everything else unchanged (including the total current) and increase the thickness of the electrodes.

The solution of the TDSE for the many-body system is obtained within Time-Dependent Current Density Functional Theory(TDCDFT) [44]; i.e., for each single-particle state ϕ_α, we have solved the equation of motion

$$\left\{ i\frac{\partial}{\partial t} - \frac{1}{2}\left(\frac{1}{i}\nabla - \frac{1}{c}\mathbf{a}_{\rm xc}\right)^2 - v_{\rm jel} - v_{\rm H} - v_{\rm xc} \right\} \phi_\alpha = 0 \tag{5.3}$$

where c is the speed of light, $v_{\rm jel}$ is the potential due to the jellium, $v_{\rm H}$ is the Hartree potential, and $v_{\rm xc}$ is the exchange-correlation scalar potential.[2] The shear viscosity of the electron liquid η enters the problem through the exchange-correlation vector potential $\mathbf{a}_{\rm xc}$ [44, 46]. If we make the appoximation that, at any given time, the viscosity is a function of the density only, and does not depend on time explicitly, we find that the $i^{\rm th}$ component of $\mathbf{a}_{\rm xc}$ evolves according to[46]

$$\frac{1}{c}\frac{\partial a_{{\rm xc},i}}{\partial t} = \frac{1}{n}\sum_j \left\{ \eta\frac{\partial^2 u_i}{\partial r_j^2} + \frac{\eta}{3}\frac{\partial^2 v_j}{\partial r_i \partial r_j} + \frac{\partial \eta}{\partial r_j}\left(\frac{\partial u_i}{\partial r_j} + \frac{\partial u_j}{\partial r_i}\right) - \frac{2}{3}\frac{\partial \eta}{\partial r_i}\frac{\partial u_j}{\partial r_j} \right\}. \tag{5.4}$$

[1] Each electrode is 51.8 Å wide in the x direction, and 22.4 Å long in the z direction of current flow (see Fig. 5.1). The width of the rectangular bridge is 2.8 Å, and the gap between the electrodes is 9.8 Å.

[2] We have used the adiabatic local density approximation to the scalar exchange-correlation potential [2, 39, 40], as derived by Ceperley and Alder [33] and parametrized by Perdew and Zunger [34].

For the viscosity η of the electron liquid we have used the one reported in Ref. 46. We employ the approach described in Refs. [13, 80, 87, 102] and in Chapters 3 and 4 to initiate electron dynamics and calculate the current. We prepare the system by placing it in its ground state; because of the applied bias, the system exhibits a separation of charge. At a time $t = 0$, we remove the bias, and let the system evolve according to eq. (5.3).[3] After long time scales, the electrons encounter the far boundaries of the jellium electrodes and reflect. However, we are interested in comparing the electron dynamics calculated from eq. (5.3) with the one obtained by solving the Navier-Stokes eqs. (5.1), at times smaller than this reflection time. Equations (5.1) are solved by assuming the same density, initial velocity and viscosity of the liquid employed in the TDCDFT calculation.[4] We also solve eqs. (5.1) assuming the liquid to be incompressible. This simplifies the calculations enormously but leads to some differences with the solutions of eq. (5.3) (see discussion later).

Fig. 5.1 depicts the flow of electrons across the nanostructure, for a range of biases between 0.02V and 3.0V, after the initial transient. The panels (a)-(d) correspond to the solution of the TDSE (eq. (5.3)); the panels (e)-(h) to the solution of the Navier-Stokes equation (eqs. (5.1)) using the same set of parameters [103]. Panel (a) has to be compared with panel (e); panel (b) with (f), and so on. As anticipated, we observe some differences between the solutions of the eqs. (5.1) and the solutions of the eq. (5.3). These differences are due to the details of the charge configuration at the electrode-junction interface, and some degree of compressibility of the quantum liquid in the junction.[5]

[3]The grid spacing of the jellium system is 0.7 Å, and the timestep used to propagate the system 2.5×10^{-3} fs. We used the Chebyshev method [48] for constructing the time-evolution operator.

[4]For the simulation of the Navier-Stokes equations we use Dirchlet boundary conditions for the velocity at the inlet, and Neumann boundary conditions at the outlet.

[5]The issue of compressibility is also related to the treatment of the fluid at the boundaries of the confining structure. In general, wavefunctions tend to exhibit exponentially decreasing density at the edges of a confining potential, while incompressible classical fluids are described with hard walls and "no-slip" boundary conditions. The assumption in the Naiver-Stokes equations that the electron liquid is incompressible also neglects the formation of surface charges; for a

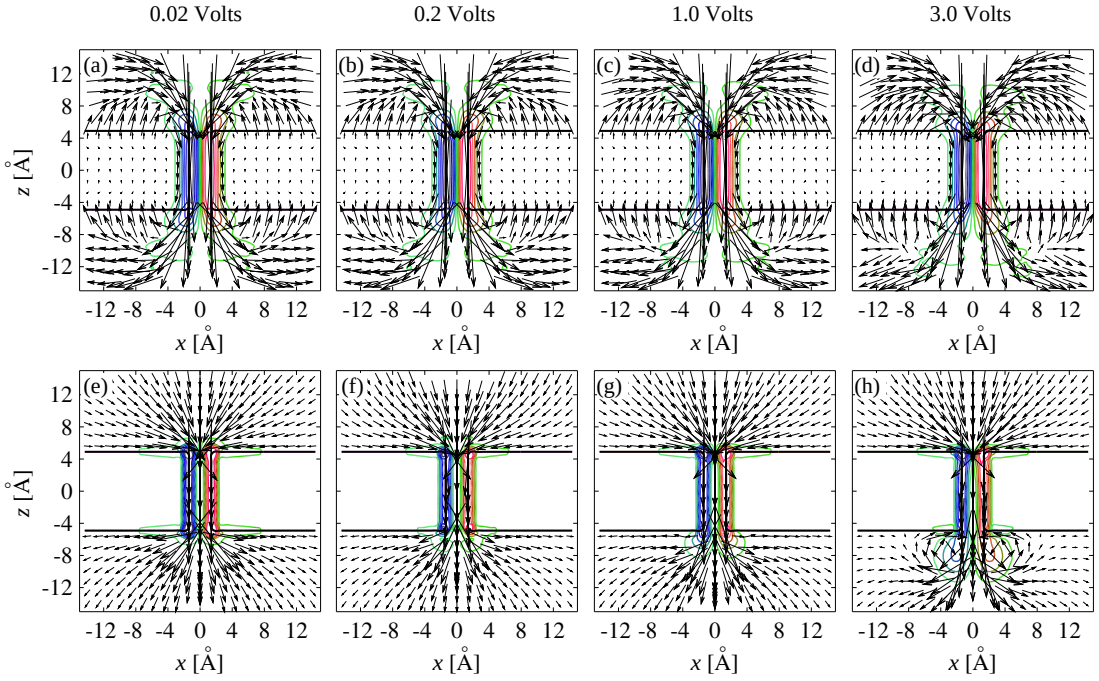

Figure 5.1 Panels (a)-(d): Electron current density for electrons moving from the top electrode to the bottom electrode across a nanojunction at $t = 1.4$ fs, for an initial bias of (a) 0.02 V, (b) 0.2 V, (c) 1.0 V and (d) 3.0 V. The arrows denote the current density, while the level sets denote the curl of the 2D current density. The solid lines delimit the contour of the junction. Panels (e)-(h): Velocity field solution of the eqs. (5.1), for a liquid with same velocity, density and viscosity as the quantum mechanical one.

From Fig. 5.1 we can see the effect of surface charges, in that some electrons flow parallel to the surfaces [102]. More importantly, at low biases, the flow is laminar and "smooth". In addition, at these biases the current density shows an almost perfect top-bottom symmetry: the direction of the flow is symmetric with respect to the operation $z \rightarrow -z$. This symmetry is even more evident by comparing the curl of the current density in the top and bottom electrodes (see for instance Fig. 5.1(a) and (e)).

By increasing the bias, however, a transition occurs: the symmetry $z \rightarrow -z$ of the current density breaks completely, and eddies start to appear in proximity to the junction. This is clearly evident, for instance, in Fig. 5.1(d) and (h). The outgoing current density in the bottom electrode has a more varied angular behavior, in contrast to the behavior in the top electrode, in which the electron liquid flows more uniformly toward the junction.

Since the panels (e)-(h) of Fig. 5.1 practically describe the dynamics of a classical fluid with the same parameters as the quantum liquid, the analogy between the electron flow and the one of a classical liquid is quite evident. We can push this analogy even further by defining a Reynolds number for the quantum system as well: $R = u_z L \rho / \eta$, where u_z is the longitudinal velocity in the junction, L is the width of the junction, and ρ is the density. Using the density of valence electrons in gold, and using the current density in the junction at $t = 1.4$ fs, we obtain for the quantum case the following Reynolds numbers: 0.216, 2.16, 10.8 and 32.5 for 0.02 V, 0.2 V, 1.0 V, and 3.0 V, respectively.

Just as in the classical case, we can then reinterpret the above results as follows. At low Reynolds numbers, the flow is highly symmetric from top to bottom. This symmetry is lost as the Reynolds number is increased. At high Reynolds numbers, the incident flow is laminar, while the outgoing flow has a jet-like character, and "turns back" on itself creating local eddies in the current density. We stress here that while the TDCDFT current density does differ, in some details, from the one

discussion of dynamical charging effects near nanoscopic junctions, see Chapter 4, or Ref. 102.

obtained from the Navier-Stokes equations, turbulent behavior (i.e. asymmetry and dynamical eddy-like formation) is observed in the fully quantum-mechanical calculation as well. The exact details of this turbulent behavior are dynamical in nature, and cannot be captured by a static calculation.

5.3 A Navier-Stokes treatment

Having shown the similarity between the current flow obtained using the Navier-Stokes equations (5.1) and the one obtained solving the TDSE (5.3) we can study the first one at times scales prohibitive for full quantum mechanical simulations. We can also study the effect of a larger thickness of the electrodes on the turbulent flow by realizing that this is equivalent to increasing the Reynolds number (which, incidentally, is also equivalent to increasing the bias). This is illustrated in Fig. 5.2 where the current density and the curl of the current density are plotted for the Reynolds number 32.5 of Fig. 5.1(h) (left panel of Fig. 5.2); same system but with a Reynolds number five times larger (middle panel of Fig. 5.2); and (right panel of Fig. 5.2) with a Reynolds number ten times larger.

From Fig. 5.2 it is evident that by increasing thickness the last remaining symmetry $x \rightarrow -x$ is broken at earlier times and closer to the junction. For instance, in the case represented in Fig. 5.2 (middle panel), the left-right symmetry is lost at about 14 fs, with consequent asymmetric flow within about 50 Å from the junction center. For the structure represented in Fig. 5.2 (right panel), the symmetry is broken at about 6 fs, and the flow asymmetry appears at about 25 Å from the junction.

We can better quantify the amount of turbulence by calculating the velocity correlation tensor [98]

$$B_{ik} = \langle (v_i(\mathbf{r}) - v_i(\mathbf{r} + \delta\mathbf{r}))(v_k(\mathbf{r}) - v_k(\mathbf{r} + \delta\mathbf{r})) \rangle \,, \tag{5.5}$$

where $\delta\mathbf{r}$ is a given distance, and $i, k = x, y, z$. Here, the angle brackets $\langle \cdots \rangle$ denote averaging over all positions $\mathbf{r}$ within a given region. Fully developed and isotropic

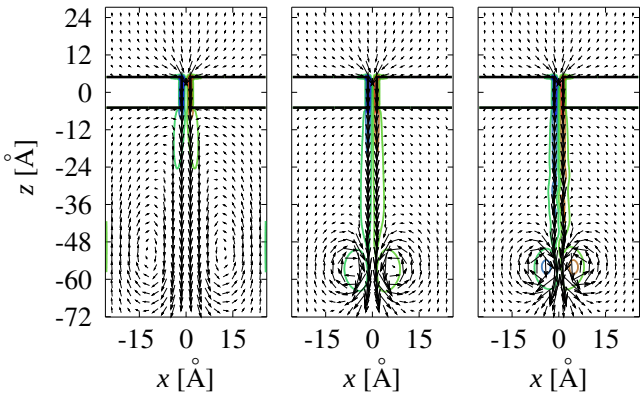

Figure 5.2 Current density (arrows) and curl of the current density (denoted by level sets) of the electron liquid, for three different Reynolds numbers, 32.5 (left panel), 162 (middle panel), and 325 (right panel). Note that the fluid velocity has lost perfect left-right symmetry in the middle- and right-panel cases.

turbulence has a velocity correlation tensor that is a function only of the magnitude of $\delta\mathbf{r}$, and increases quadratically with distance [98]. Instead, the turbulence in the examples of Fig. 5.2 is not fully developed. The velocity correlation tensor, B_{ik}, thus depends on both the magnitude of $\delta\mathbf{r}$ as well as its direction. This is illustrated in Fig. 5.3 where various components of B_{ik} are plotted at $t = 75.0$ fs for the system with Reynolds number 32.5 as a function of the magnitude of $\delta\mathbf{r}$, where we have chosen $\delta\mathbf{r}$ to point in the longitudinal (z) direction. The spatial averaging has been carried out over the left-hand side of the outgoing region (that is, in the region $z =$ [-27.3 Å, -72.1 Å], $x =$ [-25.9 Å, 0.0 Å], where the origin is in the center of the junction). For comparison, the same quantity is plotted for the laminar case, i.e. for a Reynolds number of .216. (To compare the laminar and turbulent cases we have scaled the average turbulent velocity to the average laminar velocity.) As expected, in the laminar case the correlation tensor is essentially zero, while for the turbulent case it increases with distance.

We conclude by noting that an experiment in which the electron flow can be monitored directly may measure nonlaminar electron behavior as an asymmetry between the incoming and outgoing patterns of the current density through a

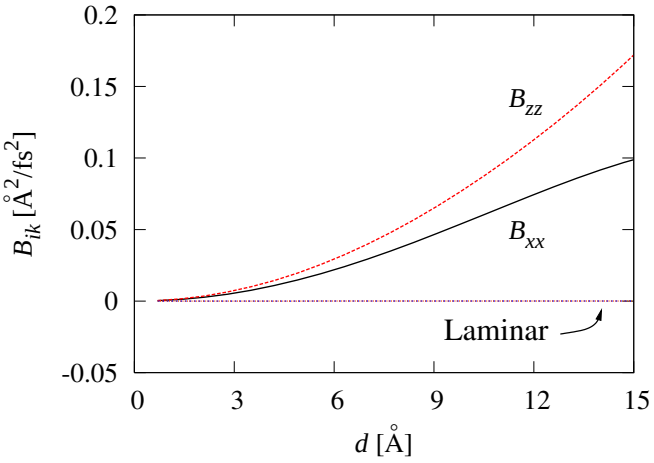

Figure 5.3 Various components of the velocity correlation tensor B_{ik} as a function of distance $d = |\delta\mathbf{r}|$, for a Reynolds number of $R = 32.5$. For the case where $R = 0.216$, the elements of B_{ik} are orders of magnitude smaller, and so the corresponding curves for the laminar case coincide with the x axis.

nanojunction. Experiments similar to the ones reported in Ref. 66, which use scanning probe microscopy to image the flowlines, may provide such capabilities. Note, however, that since these scanning probe techniques record images over time scales much longer than the turbulent electron dynamics, one would expect that in the turbulent regime images of current flow appear "smeared out" compared to the laminar case, and asymmetric in the incoming and outgoing patterns. One can also envision the possibility of using the magnetic field produced by the current to probe the electrons' transition to turbulence: the magnetic field on the top electrode would be different from the magnetic field in the bottom electrode (turbulent region). We will explore this possibility in Chapter 6. From the present work and the analytical results obtained in Ref. 95, we also suggest that fully 3D and non-adiabatic junctions, i.e. junctions with a geometry that changes abruptly (like the one explored in this Chapter), are the best candidates to observe turbulence. We also expect defects and other impurities to favor turbulent behavior by playing the role of "obstacles" for the electron flow.

We finally note that turbulent behavior may have consequences on the forma-

tion (or lack thereof) of local equilibrium distributions in the electrodes [80] (see Chapter 3), and may generate non-trivial local electron heating effects in the junction [104] and at the eddies sites. These phenomena and properties are still poorly understood at the nanoscale and ultimately may have unexpected consequences on the stability of nanostructures under current flow [105–107].

ACKNOWLEDGEMENTS

We acknowledge useful discussions with Roberto D'Agosta. One of us (JG) received support from the National Science Foundation's REU program. This work was supported by the U.S. Department of Energy under grant DE-FG02-05ER46204.

Chapter 5 is a reprint of the material as it appears in Neil Bushong, John Gamble and Massimiliano Di Ventra, "Electron turbulence at nanoscale junctions," *Nano Letters* **7**, 1789 (2007). Copyright 2007 by the American Chemical Society. The dissertation author was the primary investigator of this paper.

6

Turbulence-induced magnetic flux asymmetry at nanoscale junctions

6.1 Introduction

The hydrodynamics of the electron liquid dates back to earlier studies by Madelung, Bloch [108, 109] and later on by Martin and Schwinger [92]. In this latter work in particular, it was shown that the many-body time-dependent Schrödinger equation (TDSE) can be written exactly in hydrodynamic form in terms of the density $n(\mathbf{r},t)$ and velocity field $\mathbf{v}(\mathbf{r},t) = \mathbf{j}(\mathbf{r},t)/n(\mathbf{r},t)$, where $\mathbf{j}(\mathbf{r},t)$ is the current density, with all many-body interactions lumped into a two-particle stress tensor.

In recent years, the analogy of the electron flow with classical fluid dynamics has been pushed even further with the development of time-dependent density-functional methods and the consequent realization that under certain conditions, the exchange-correlation potentials can be written in hydrodynamic form [44, 94]. More recently, it was shown that electron flow in nanoscale constrictions satisfies the conditions to write the two-particle stress tensor in a form similar to the stress tensor of the Navier-Stokes equations with an effective viscosity of the electron liquid (see also below) [95]. The most striking prediction of this result is that, under specific conditions on the current, density and junction geometry, the electron flow

should undergo a transition from laminar to turbulent regimes [95]. Recently, this behavior was confirmed numerically by solving directly the TDSE within time-dependent current-density functional theory [110] and comparing the results with the generalized Navier-Stokes equations derived in Ref. 95. (See Chapter 5.) In experiments, however, detecting turbulence via direct imaging of the current density remains challenging. For instance, scanning-probe microscopy (SPM) experiments which image the current flow in a 2D electron gas (2DEG) have been reported [66]. These experiments employ an SPM tip to reflect electrons back toward the junction, and measure the resultant change in the total current. This means that the image thus obtained gives the correlation between the tip position and junction current, which does not necessarily correspond to the magnitude of the current density. Moreover SPM-type experiments are essentially invasive. Another way to probe turbulence would be to measure the noise properties of the current. However, this would lead to difficulties in interpreting the data, due to the analytical intractability of turbulence and correlations with other types of noise [69].

In the present chapter we show that the measurement of the current-induced magnetic field at the two sides of an otherwise symmetric nanojunction provides a direct and non-invasive way of measuring the transition from laminar to turbulent flow. In particular, we predict that the fluxes ensuing from the current-induced magnetic field across two surfaces on the two sides of the junction would at first become increasingly different with increasing current. This asymmetry reaches a maximum, and then decreases with further increase of the current. The measurement of these fluxes is within reach of present experimental capabilities, and thus the observation and study of this phenomenon would provide valuable insight into the transport properties of nanoscale systems.

6.2 System configuration

The structure we have in mind consists of two symmetric regions of a 2DEG connected *non-adiabatically* by a nanojunction (the edges of this structure are rep-

resented with solid lines in the left panel of Figs. 6.1 and 6.2). The non-adiabaticity requirement is due to the fact that, as shown in Ref. 95, an adiabatic constriction produces a Poiseuille flow, which is laminar for essentially all currents one can effectively inject in a 2DEG.[1] The lateral (y-direction) boundaries are closed to current flow, and the longitudinal (x-direction) boundaries are open, with current being injected in the "top" boundary and exiting in the "bottom" boundary. We then envision two identical surfaces – placed at a given distance from the 2DEG in the z direction – across which we calculate the current-induced magnetic flux (see Fig. 6.1). These magnetic fluxes can be measured by two superconducting quantum interference devices (SQUIDs) [111] located on the two sides of the junction as illustrated in Fig. 6.1.

Our starting point is the time-dependent Schrödinger equation written in the approximate Navier-Stokes form for an incompressible fluid [95]

$$\begin{aligned} D_t n(\mathbf{r},t) = 0,\ \nabla\cdot\mathbf{v}(\mathbf{r},t) = 0, \\ m^* n(\mathbf{r},t) D_t v_i(\mathbf{r},t) = -\frac{\partial}{\partial r_i} P(\mathbf{r},t) + \eta\nabla^2 v_i(\mathbf{r},t) \\ - n(\mathbf{r},t)\frac{\partial}{\partial r_i} V_{\rm ext}(\mathbf{r},t) \end{aligned} \tag{6.1}$$

where $D_t = \frac{\partial}{\partial t} + (\mathbf{v}\cdot\nabla)$ is the convective derivative, m^* is the effective mass of the electrons, $n(\mathbf{r},t)$ is the electron density, $P(\mathbf{r},t)$ is the pressure of the electron liquid, and $V_{\rm ext}(\mathbf{r},t)$ is the sum of the Hartree and the ionic potentials. The quantity $\eta = \hbar n f(n)$ is the viscosity of the electron liquid, with $f(n)$ a smooth function of the density. The values of the viscosity as a function of density have been calculated using linear-response theory [46, 112]; here, we use the 2D interpolation formula of Ref. 46. We also employ the jellium approximation for the electron liquid, which together with the assumption of incompressibility, allows us to neglect spatial variations of $V_{\rm ext}(\mathbf{r},t)$. Incompressibility of the electron liquid represents to a good approximation the behavior of metallic quantum point contacts[2] [95, 110].

[1] Note that if turbulence is observed in a 2D system at a given current, turbulence is even more favored in 3D at the same current.

[2] Incompressibility neglects the formation of surface charges near the edge of the gap between

The current density was calculated numerically as a solution of Eqs. (6.1) [103] for a nanojunction 28 nm wide. We have used Dirichlet boundary conditions for the velocity at the inlet, and Neumann boundary conditions at the outlet, and we have used "slip" boundary conditions for the walls. We use parameters corresponding to a GaAs-based 2DEG: $m^* = 0.067 m_e$, and $n = 5.13 \times 10^{11}\,\mathrm{cm}^{-2}$. The calculations were performed at a fixed value of the total current flowing through the system selected in the range from $0.001\,\mu$A to $10\,\mu$A. The magnetic field profile was found for each calculated current density distribution. The size of the surface area across which we calculated the magnetic flux was chosen to be 200×200 (nm)^2. Each surface is displaced laterally to one side of the nanojunction as shown in Fig. 6.1. This surface represents the SQUID area and, in principle, does not necessarily need to be so small. We assume that the surfaces are located 50 nm above the 2DEG; therefore, the distributions of magnetic field were calculated at this distance from the 2DEG.[3] For convenience, from now on we shall call these two surfaces SQUID 1 and SQUID 2 (Figs. 6.1 and 6.2).

6.3 Magnetic flux asymmetry

The magnetic field fluxes allow us to characterize the degree of asymmetry in the current flow pattern as well as to probe such specific features of turbulent current flow as eddies. We find that at low currents, the electron flow pattern is symmetric (see left panel of Fig 6.1). More precisely, the patterns of current flow in the two electrodes are mirror images of each other, with the overall sign of the flow reversed [110]. This is illustrated in the left panel of Fig. 6.1, where we

the contacts [91, 102, 110]. (See Chapter 4.) These charges form dynamically during the initial transient of the current, and during that time create a displacement current, which would affect the initial-time magnetic field. However, this surface charge distribution is stationary after the transient, and therefore it does not influence the long-time behavior of the magnetic field.

[3] One can estimate the decrease of the magnetic flux with distance by considering the flux through a square SQUID of side l created by a current in a wire located at a distance h beneath a SQUID side. It can be shown that the magnetic field flux $\phi \sim \mathrm{Log}(1 + h^2/l^2)$. Taking $l = 200$ nm, $h_1 = 50$ nm and $h_2 = 100$ nm we obtain the flux ratio of 1.76.

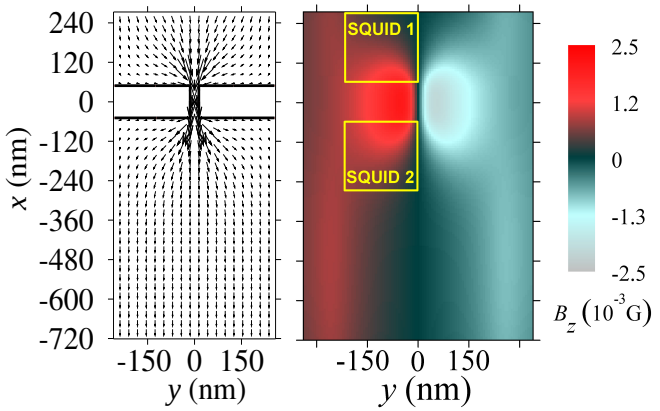

Figure 6.1 Laminar current flow at a low value of the total current (0.1 μA). Left panel: electron velocity distribution. The arrow length is proportional to the velocity magnitude. Right panel: normal component of the magnetic field through a plane 50 nm above the 2DEG. The surface areas indicated with SQUID 1 and SQUID 2 represent two areas across which we calculate the magnetic flux (see text).

plot the velocity distribution of the electron liquid at a simulation time of 24 ps. The total current is 0.1 μA, which is small enough that the flow is in the laminar regime, as it is evident from the figure. In the right panel of Fig. 6.1, we show the z-component of the magnetic field through a plane 50 nm above the 2DEG. As is typical of the laminar regime, the current-induced magnetic fields above the top and bottom contacts are almost symmetric with respect to the center of the junction producing an almost symmetric flux across the areas. Hence, SQUIDs positioned as indicated in Fig. 6.1 would measure almost equal magnetic fluxes.

By increasing the current, the current density in the source and drain sides loses top-down symmetry: the current density in the outgoing side becomes turbulent, while the current density in the incident side remains laminar (Fig. 6.2). We note that at large currents we observe the formation of turbulent "eddies" which evolve in time, rather than a completely chaotic current density distribution. This means that, at the current values we consider here, turbulence is not fully developed [110].

Fig. 6.2 illustrates the behavior typical for the turbulent regime. This plot

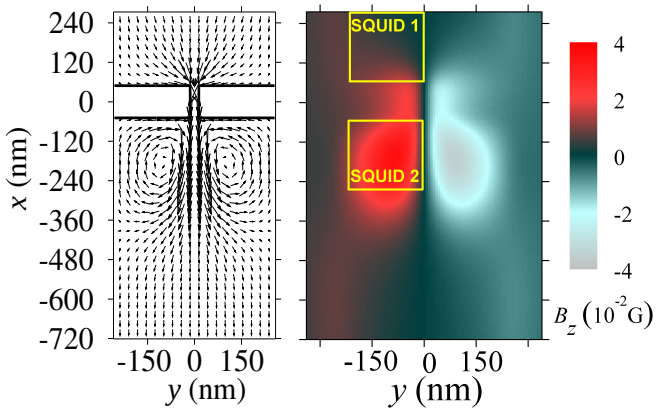

Figure 6.2 Turbulent current flow at high value of the total current (1 μA). Left panel: electron velocity distribution. Right panel: normal component of the magnetic field through a plane 50 nm above 2DEG. The top-down symmetry in magnetic field distributions across the SQUID areas is lost. The magnetic field flux through SQUID 2 is significantly higher then the flux through SQUID 1.

corresponds to a total current of 1.0 μA at time $t = 24$ ps. As before, the left panel shows the electron velocity distribution. Unlike the electron velocity field presented in Fig. 6.1, the electron velocity distributions in the top and bottom electrodes in Fig. 6.2 are no longer symmetric. In particular, the electron velocity distribution in the bottom contact shows eddies and an increased current density in the middle of the junction. Such a velocity field is responsible for a much stronger magnetic field in the SQUID 2 area. In contrast, the magnetic field distribution in the SQUID 1 area in Fig. 6.2 is "smooth" and uniform, and has a structure similar to the magnetic field distribution in the SQUID 1 area of Fig. 6.1.

For both the laminar and turbulent cases, as time passes, the fluxes through the top and bottom SQUID areas saturate to constant values. This is shown in the inset of Fig. 6.3 where we plot the flux through the top and bottom SQUID areas as a function of time for the 1.0 μA case. We can now determine the magnetic signature of the transition between the laminar and turbulent regimes by plotting the asymptotic value of the ratio of the magnetic fluxes through the two SQUID areas as a function of the total current. This is illustrated in Fig. 6.3 and shows

the main findings of this chapter.

At low currents (i.e., the laminar regime), the current density in the top and bottom electrodes is highly symmetric. Therefore, the ratio of the fluxes Φ_2/Φ_1 is near unity.[4] The upper electrode remains laminar regardless of the magnitude of the current which is typical of systems with narrow constrictions [98]. Increasing the current gives rise to the formation of eddies in the bottom electrode, which leads to an enhanced magnetic field due to the circular character of the current density. However, as the current is increased further, the eddies spread and move "downstream." The decreased proximity of the center of the eddy to the SQUID has the effect of decreasing the measured flux. (Despite this effect, the ratio Φ_2/Φ_1 is still much higher than in the laminar case.) The range near 1.0 μA is an optimal regime, where eddies form and remain localized near the junction. The Reynolds number $Re = 156$ corresponding to the total current of 1μA can be considered as the critical Reynolds number Re_{crit}. This critical value, which depends only on the geometry of the junction, is comparable to the critical value found in other systems making similar transitions [98].

The inset of Fig. 6.3 gives the magnetic flux measured by each SQUID, as a function of time, for a current of 1.0 μA. As the eddies form, the flux measured by SQUID 2 climbs well above the value measured by SQUID 1, eventually reaching a stable value of $5.4 \times 10^{-5}\Phi_0$, where $\Phi_0 = h/2e$ is the magnetic flux quantum. The fast rise of the fluxes is due to the fast formation and propagation of the eddies along the junction. The noise level of modern SQUIDs [113] is below $10^{-6}\Phi_0$, which is well below this asymptotic flux magnitude.

6.4 Additional considerations

We conclude by quantifying the degree of turbulence of the current-induced magnetic field. While this cannot be directly measured, it provides insight into the

[4]The flux ratio is expected to approach unity in the limit of zero current and infinite systems.

properties of the turbulent regime attainable experimentally. Let us then calculate the magnetic field correlation tensor, which quantifies the spatial correlation of the magnetic field at different points in space. We define this tensor as

$$C_{ij} = \langle (B_i(\mathbf{r}) - B_i(\mathbf{r}+\delta\mathbf{r}))(B_j(\mathbf{r}) - B_j(\mathbf{r}+\delta\mathbf{r}))\rangle \,. \tag{6.2}$$

Here, B_i and B_j denote components of the magnetic field, and $\delta\mathbf{r}$ is a given vector. The brackets $\langle \ldots \rangle$ denote averaging over all pairs of positions separated by $\delta\mathbf{r}$ within a given region. Note that, even before performing a spatial average, the magnetic field already has a nonlocal character, in that the magnetic field at a point is due to the velocity of charges in the whole system.

In Fig. 6.4 we plot the magnetic field correlation tensor C_{zz}, for $\delta\mathbf{r} = (\delta x, 0)$ at 50 nm above the 2DEG as a function of δx. The spatial averaging was carried out in a region "downstream" from the junction, in the region $x = [-487\,\mathrm{nm}, -235\,\mathrm{nm}]$, $y = [0\,\mathrm{nm}, 259\,\mathrm{nm}]$. As expected, in the laminar case, the magnetic field varies with distance by a small amount, so that C_{zz} is small. In the turbulent case, the presence of the eddies leads to a magnetic field that correlates spatially, causing C_{zz} to increase with distance.

Finally, we discuss some possible alternatives to measuring turbulence via the proposed magnetic fluxes. Instead of using two SQUIDs placed at the two sides of the junction one could envision the use of only one SQUID, and changing the direction of current flow by merely reversing the bias. This also ensures that the effect of unavoidable scattering by defects/impurities on the magnetic fluxes is accounted for identically for both possible directions of overall current flow. Another alternative is to use a movable SQUID [114, 115] or scanning Hall-probe microscopy [116], in order to generate images of the magnetic flux as a function of position. Imaging electron flow in this way would provide information about the electric current density throughout the device with the added benefit that the measurement would be noninvasive.[5] However, we expect scanning SQUID

[5]Extracting the current density from the magnetic field is a nontrivial problem, but has been heavily studied; for an example in the context of medicine, see Ref. 117.

microscopy to have a lower sensitivity due to the increased distance between the SQUID and the sample.

One can also tune the critical current value at which the transition between laminar and turbulent regimes occurs by using materials with different effective masses. For example, the heavy-hole effective mass in p-doped GaAs is about $0.45m_e$, which implies that the transition to turbulent flow in p-doped GaAs should occur at $I_{\mathrm{c}}' = (0.067/0.45) * I_{\mathrm{c}} = 0.047\,\mu\mathrm{A}$ for the same doping density as the n-doped case.

ACKNOWLEDGEMENTS

This work was supported by the U.S. Department of Energy under grant DE-FG02-05ER46204. We are thankful to S. N. Shevchenko for useful information regarding SQUIDs.

Chapter 6 is a reprint of the material as it appears in Neil Bushong, Yuriy Pershin and Massimiliano Di Ventra, "Turbulence-induced magnetic flux asymmetry at nanoscale junctions," *Physical Review Letters* **99**, 226802 (2007). Copyright 2007 by the American Physical Society. The dissertation author was the primary investigator of this paper.

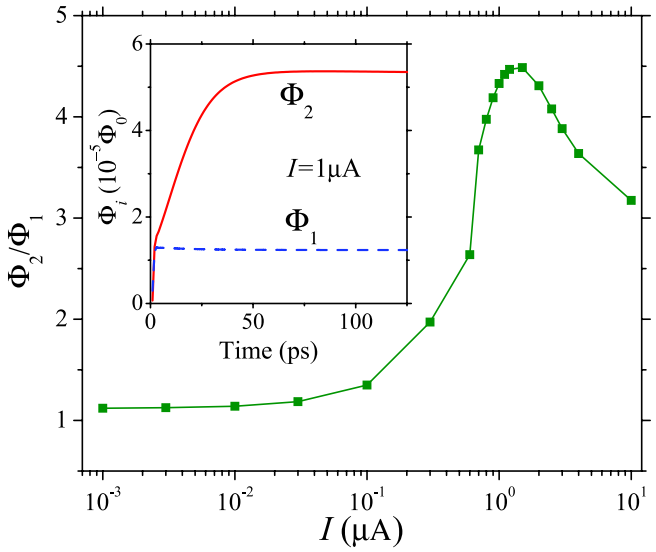

Figure 6.3 Asymptotic value of the ratio of the flux through SQUID 2 area to the flux through the SQUID 1 area as a function of the total current. See text for details. *Inset*: Time dependence of fluxes (in units of $\Phi_0 = h/2e$) through the top (dashed blue line) and the bottom (solid red line) SQUID areas, for a total current of 1.0 μA.

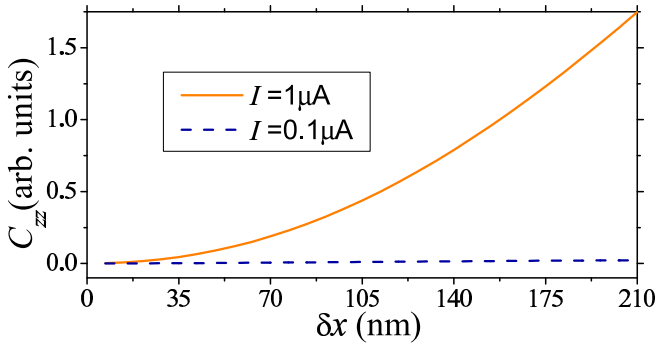

Figure 6.4 Magnetic field correlation function, for total currents of 1.0 μA (solid orange curve) and 0.1 μA (dashed blue curve). Because the total current differs between the two by a factor of 10, we have scaled the 0.1 μA curve by a factor of 10^2. Even after this scaling, C_{zz} is significantly larger in the turbulent (high-current) case than it is in the laminar (low-current) case.

7

The decay of excited He from Stochastic Density-Functional Theory: a quantum measurement theory interpretation

7.1 Introduction

Density-functional theory (DFT), in both its ground-state and time-dependent versions [1, 2, 39, 42, 118] has become the method of choice to study several equilibrium and non-equilibrium properties of interacting many-particle systems evolving under Hamiltonian dynamics.

There is, however, a large class of physical problems where the dynamical interaction of a quantum system with an external environment needs to be taken into account. To this class of *open quantum systems* belongs also one of the most basic tenets of Quantum Theory, namely the non-unitary evolution of a quantum state due to the measurement by an apparatus. Non-unitary quantum evolution also pertains to processes where the energy of the quantum system relaxes into the degrees of freedom of a bath or reservoir, like, e.g., the decay of exited systems. An

understanding of such processes from a microscopic point of view would represent a substantial advancement in the study of open quantum systems.

To address the above issues, Di Ventra and D'Agosta (DD) have recently proved [112] that given an initial quantum state, and an operator $\hat{V}$ that describes the interaction of a many-body system with an external environment, two external vector potentials $\mathbf{A}(\mathbf{r},t)$ and $\mathbf{A}'(\mathbf{r},t)$ that produce the same ensemble-averaged current density, $\overline{\mathbf{j}(\mathbf{r},t)}$, must necessarily coincide, up to a gauge transformation. The DD theorem thus extends the previous theorems of dynamical DFT (that are one of its corollaries if $\hat{V}=0$), and allows for the first-principles description of the dynamics of open quantum systems via effective single-particle equations. This theory has been named Stochastic Time-Dependent Current-DFT (Stochastic TD-CDFT).

Here we apply the above theory to a previously inaccessible problem via standard DFT methods: the decay of an ensemble of excited He atoms. In addition, we interpret the results in the context of quantum measurement theory by showing that the interaction with the environment can be viewed as a continuous "measurement" of the state of the system, thus making a connection between density-functional theory and quantum measurement theory.

We consider two cases: 1) an ensemble of excited He^+ atoms, whose dynamics can be directly compared with the one obtained from a density-matrix approach. 2) An ensemble of neutral excited He atoms. Our results reveal unexpected features of this problem, like the dampening and modification of high-frequency oscillations during energy relaxation of the ensemble towards its ground state.

The starting point of Stochastic TD-CDFT is the stochastic equation of motion of an auxiliary Kohn-Sham (KS) Slater determinant Ψ^{KS} built out of single-particle KS states ϕ_α

$$\begin{aligned}\partial_t\Psi^{KS}(t) = &-\mathrm{i}\sum_i \hat{H}_i^{KS}(t)\Psi^{KS}(t) - \frac{\tau}{2}\hat{V}^\dagger\hat{V}\Psi^{KS}(t)\\ &+\ell(t)\hat{V}\Psi^{KS}(t)\,,\end{aligned} \tag{7.1}$$

where

$$\hat{H}_i^{KS}(t) = \frac{[\hat{p}_i + \mathbf{A}(\hat{r}_i,t)/c + \mathbf{A}_{xc}(\hat{r}_i,t)/c]^2}{2} + \hat{V}_H(\hat{r}_i,t)\,, \tag{7.2}$$

with $\mathbf{A}(\hat{r}_i,t)$, an arbitrary external vector potential, $\mathbf{A}_{xc}[\overline{\mathbf{j}(\mathbf{r},t)},|\Psi_0\rangle,\hat{V}]$ the exchange-correlation vector potential (which is a functional of the average current $\overline{\mathbf{j}}$, the initial condition $|\Psi_0\rangle$, and the operator $\hat{V}$), and $\hat{V}_H(\mathbf{r},t)$ the Hartree potential. The quantity τ has dimensions of time. Without loss of generality the stochastic process, $\ell(t)$, is chosen such that it has both zero ensemble average and $\delta-$autocorrelation, i.e.,[1]

$$\overline{\ell(t)} = 0;\ \overline{\ell(t)\ell(t')} = \tau\delta(t-t')\,, \tag{7.3}$$

where the symbol $\overline{\cdots}$ indicates the average over a statistical ensemble of identical systems all prepared in the same initial quantum state $|\Psi_0\rangle$. For the particular choice of bath operator we will make in this chapter (Eq. (7.5)), which acts on single-particle states only, the stochastic equation (7.1) is simply

$$\partial_t\phi_\alpha(t) = -\mathrm{i}\hat{H}_{\mathrm{KS}}\phi_\alpha(t) - \frac{\tau}{2}\hat{V}^\dagger\hat{V}\phi_\alpha(t) + \ell(t)\hat{V}\phi_\alpha(t)\,, \tag{7.4}$$

where α contains also the spin degrees of freedom.

The use of a stochastic Schrödinger equation in the context of DFT, and not of an equation of motion for the density matrix, is because in DFT the KS Hamiltonians depend on the density (and/or the current density), and therefore they are, in general, different for the different elements of the ensemble. This does not generally guarantee a closed equation of motion for the single-particle KS density matrix of the mixed state [112].

7.2 Decay of a He^+ ion

As mentioned previously, our aim is to describe the decay of excited electrons bound to a He nucleus. The electrons are prepared in some initial excited state,

[1] In the calculations of this chapter, we use small but finite time steps of duration Δt. The mean and autocorrelation of $\ell(t)$ are thus given by $\overline{\ell(t_i)} = 0$ and $\overline{\ell(t_i)\ell(t_j)} = \delta_{i,j}\tau/\Delta t$, respectively, where t_i and t_j are arbitrary times, and $\delta_{i,j}$ is the Kronecker delta. We have chosen the probability distribution $P(\ell)$ of $\ell(t)$, to be Gaussian, so that $P(\ell) = \sqrt{\Delta t/2\pi\tau}\exp(-\ell^2\Delta t/2\tau)$.

and evolve into the ground state as a result of the stochastic interaction with an environment, that, quite generally, can be thought of as a boson field. The precise form of the operator $\hat{V}$ which causes this behavior would, in general, depend on the detailed model of the environment. Here we choose the simplest possible operator, whose matrix elements are[2]

$$\langle \epsilon_i | \hat{V} | \epsilon_j \rangle = \begin{cases} 1/\sqrt{\tau t_{\rm d}} & \text{if } i = 0, \text{ and } 0 < j < M \\ 0 & \text{otherwise,} \end{cases} \tag{7.5}$$

where $|\epsilon_i\rangle$ is an eigenstate of the ground-state KS Hamiltonian in the absence of the interaction with the bath, ϵ_i is the corresponding eigenvalue, and the upper limit M is a given integer representing the number of states we keep in the simulation. (In the present case we have kept $M = 15$ states.) The parameter $t_{\rm d}$ gives the timescale over which the decay will occur, with larger values of $t_{\rm d}$ leading to longer decay times.[3] In the following we have chosen $t_d = 1$ fs. The operator $\hat{V}$ defined this way ensures that the stochastic Schrödinger equation (7.4) is independent of the magnitude of τ.

Clearly, the above operator reduces the projection of a wave-function from the states $\{|\epsilon_1\rangle, |\epsilon_2\rangle \ldots |\epsilon_{M-1}\rangle\}$, and increases the projection onto the ground state $|\epsilon_0\rangle$. Physically, it describes energy relaxation and dephasing.

The stochastic Schrödinger equation (7.4) preserves the ensemble-averaged wave-function normalization [112]. However, the normalization is not necessarily satisfied for any particular realization of $\ell(t)$. In order to reduce the number of dynamical calculations to perform the ensemble average, we have explicitly re-normalized $|\phi\rangle$ at every time step. As we will see below, with this approximation the decay into the ground state is evident even after a single realization of ℓ.[4]

We begin by considering the behavior of an ensemble of He^+ ions interacting

[2]In our numerical work we have used a position basis so that the action of this operator in this basis is $\langle \mathbf{r}|V\psi(t)\rangle = \sum_i \langle \mathbf{r}|\epsilon_i\rangle \sum_j \langle \epsilon_i|V|\epsilon_j\rangle\langle \epsilon_j|\psi(t)\rangle = \langle \mathbf{r}|E_0\rangle \frac{1}{\sqrt{\tau t_{\rm d}}} \sum_{j=1}^{j<M} \langle \epsilon_j|\psi(t)\rangle$.

[3]In Ref. 119, a similar operator for a two-state system is provided to describe energy relaxation and decoherence.

[4]Nevertheless, this creates slight differences in the long-time limit of the dynamics with respect to the exact solution (see, e.g, Fig. 7.1).

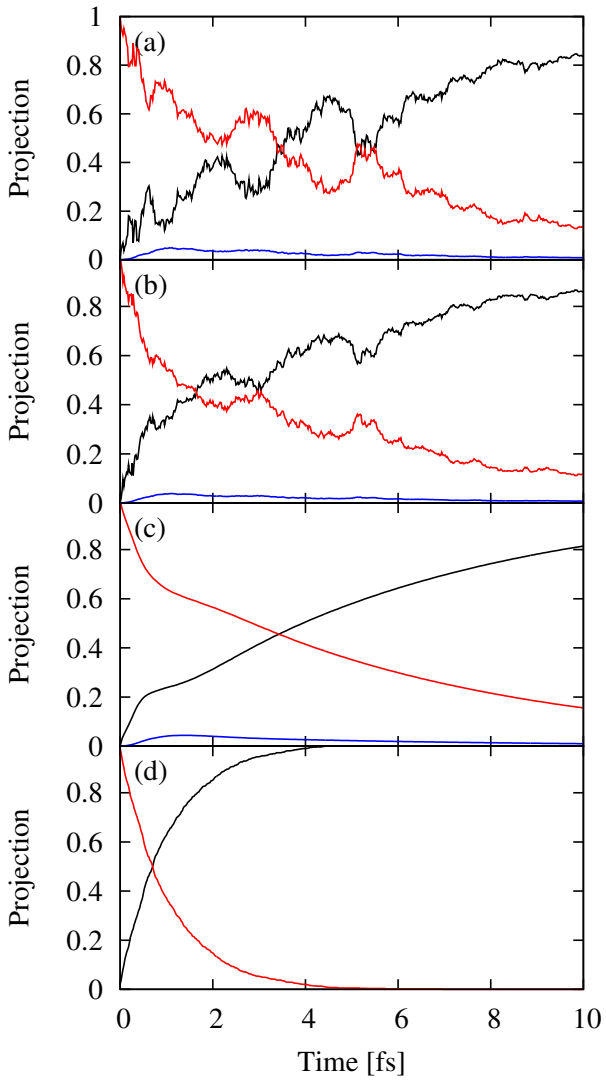

Figure 7.1 *Panel (a):* Stochastic evolution of the projections P_i onto the unperturbed states ϵ_i, for He^+, as a function of time. The solid black, dashed red, and dotted blue curves correspond to P_0, P_1, and P_2, respectively. Note that the projections P_3 and P_4 coincide with P_2, since all three states have p symmetry. All other projections are vanishingly small. *Panel (b)* Same as for panel (a), but averaged over five different runs, each with a different seed for the random number generator. *Panel (c):* Same as for panels (a) and (b), except that the dynamics were calculated using the Lindblad master equation (7.6). *Panel (d):* Same as for panels (a)-(c), except the dynamics were calculated using the wave-packet collapse methodology of equation (7.7).

with the environment represented by the operator (7.5). We prepare the system with all ions in the ensemble in the 2s state, denoted by $|\epsilon_1\rangle$, and then let the electrons evolve in time according to equation (7.4).[5] Panel (a) of Fig. 7.1 gives the projections $P_i(t) = |\langle\epsilon_i|\phi(t)\rangle|^2$, as a function of time for one particular realization of $\ell(t)$. We see that the projection $P_0(t)$ onto the ground state approaches one as time evolves, while the projections onto other states approach zero, indicating energy relaxation into the ground state. In order to demonstrate that this behavior is not due to the particular choice of seed in our random number generator, we also plot the projections $P_i(t)$ averaged over 5 different simulations with different seeds. One can clearly see that the fluctuations in panel (b) of Fig. 7.1 are reduced in comparison to the fluctuations in panel (a).

For the single-electron case of He^+, we can analytically treat the ensemble average over all realizations of $\ell(t)$ by considering the density matrix of this mixed state. Using equations (7.4) and (7.3), it can be shown [112, 119] that the resultant density matrix $\hat{\rho}$ evolves according to the Lindblad master equation

$$\frac{\mathrm{d}\hat{\rho}}{\mathrm{d}t} = -\mathrm{i}[H_{\mathrm{KS}}, \hat{\rho}] + \tau V\hat{\rho}V^\dagger - \frac{\tau}{2}\hat{\rho}V^\dagger V - \frac{\tau}{2}V^\dagger V\hat{\rho}\,. \tag{7.6}$$

In panel (c) of Fig. 7.1 we plot the matrix elements $\langle\epsilon_i|\hat{\rho}|\epsilon_i\rangle$ showing the same behavior obtained with Eq. (7.4).[6]

We now discuss this result in terms of measurement theory. It is well-known that is possible to interpret the interaction with an environment as a continuous "measurement" of the state of the system – or, equivalently, of the state of the environment – with consequent non-unitary wave-packet reduction [122, 123]. We

[5] We represent the He nucleus with a simple $2/r$ potential. We integrate out the singularity at the origin using a method similar to the Ewald method [120, 121]. We use the Hockney method to calculate the potential of an isolated system [89]. The supercell is a cube of length 16.93 Å, and the grid spacing is 0.239 Å. We use the Chebyshev method of constructing the propagator [48, 49], and we use a time step of 0.02 fs.

[6] Note that the density matrix procedure we have used here does not take into account the additional re-normalization that we apply in order to speed convergence in the calculations with Eq. (7.4). The close correspondence between panels (b) and (c) in Fig. 7.1 demonstrates that our forced normalization procedure does not cause significant deviation from the true average behavior of the system.

can make this point even clearer by assuming that every time the system interacts with the environment it emits a boson excitation (whether a photon or a phonon) and thus there is a finite probability $\mathrm{d}p = \mathrm{d}t|\langle\epsilon_1|\psi\rangle|^2/t_d$ that the the emitted excitation be detected by an apparatus [124]. Upon detection of this excitation, the wave-function $|\phi\rangle$ *collapses* to the ground state $|\epsilon_0\rangle$. This is the well-known postulate of wave-packet reduction.

We can write the above in the form of a Schrödinger-type equation of motion that includes a stochastic variable $\gamma(t)$, which has a probability distribution uniformly distributed between 0 and 1. If $\gamma > \mathrm{d}p$, an emitted excitation is not detected, while if $\gamma < \mathrm{d}p$, the emitted excitation is detected, and the wavefunction collapses to the ground state. That is, during a small time Δt, $|\phi\rangle$ evolves according to

$$\begin{aligned} |\phi(t+\Delta t)\rangle = \mathrm{e}^{-\mathrm{i}H_{\mathrm{KS}}\Delta t}\theta(\gamma(t)-\mathrm{d}p)|\phi(t)\rangle \\ + \theta(\mathrm{d}p-\gamma(t))|\epsilon_0\rangle\,, \end{aligned} \tag{7.7}$$

where $\theta(x)$ is the Heaviside step function.[7] A similar approach has been used by Dalibard *et al.* in the context of quantum optics [124].

In Fig. 7.1(d), we plot the results from the time evolution of equation (7.7) for the problem of He^+ relaxation, where we have considered only the ground state and the first excited state. Starting with $|\phi(t=0)\rangle = |\epsilon_1\rangle$, we evolved equation (7.7) in time for 1000 different realizations of $\gamma(t)$, and found the average value of $|\langle\epsilon_i|\phi(t)\rangle|^2$, which we have denote by P_i. Note that each individual wave-function starts in the excited state, and then suddenly drops to the ground state the first time that $\gamma(t) < \mathrm{d}p$. This wave-packet reduction occurs at a different time for each run, and the "remaining" excited states become exponentially less likely as time goes on; therefore, the average curve approaches an exponential. By comparing Fig. 7.1(d) with Fig 7.1(c) we see that the non-unitary wave-packet reduction evolution is qualitatively similar to that provided by the stochastic Schrödinger

[7] It can be shown [124] that by defining an operator $\hat{S}$ such that $\hat{S}|\epsilon_1\rangle = |\epsilon_0\rangle$, the density matrix $\hat{\rho}$ associated with Eq. (7.7) satisfies the Lindblad equation (7.6) with $\hat{S}$ replacing $\hat{V}$.

equation (7.4), the difference being in the fact that we have included only two states in the analysis of Eq. (7.7). This equivalence therefore illustrates a point of contact between the stochastic Schrödinger equation (7.4) and quantum measurement theory. The environment "measures" the state of the system, and, as a result, the wave-function is modified in a non-unitary way.

7.3 Decay of a neutral He atom

We conclude by discussing the decay of neutral He, where a closed form for the KS single-particle Lindblad equation cannot be obtained. We prepare the system in such a way that both electrons (with spin σ) are in the first excited state $|\psi_\sigma(t=0)\rangle = |\epsilon_1\rangle$. This means that the Pauli exclusion principle is automatically satisfied by our environment operator (7.5). For this case we compare the stochastic evolution with the one in which $\hat{V} = 0$.[8]

In Fig. (7.2), we plot the projections $P_i = |\langle\epsilon_i|\psi\rangle|^2$ for the unitary evolution (panel (a)), as well as the projections for the non-unitary evolution for one realization of $\ell(t)$ (panel (b)) and averaged over five different realizations of $\ell(t)$ (panel (c)). As expected, in the presence of the environment, the projection onto the ground state $|\epsilon_0\rangle$ approaches 1, while the occupations of other states are suppressed as time goes on. Here, however, we also note another effect of the interaction. Fig. 7.2(a) illustrates that, in the unitary evolution the projections P_i oscillate in time. This oscillatory behavior reflects the motion of the electrons as they alternately fall toward the nucleus, and then rebound outward.[9] Interaction with the environment has the effect of not only dampening these oscillations but also of modifying their frequency, the details of which vary depending on the particular realization of $\ell(t)$. The introduction of the bath mediates new transitions

[8] We use the local density approximation to the scalar exchange-correlation potential [2, 39], as derived by Ceperley and Alder [33] and parametrized by Perdew and Zunger [34]. For the current-density functional, we use the interpolation formula of Conti and Vignale [46].

[9] Sugino *et al.* report similar high-frequency oscillations while studying the dipole moment of an isolated aluminum dimer [125].

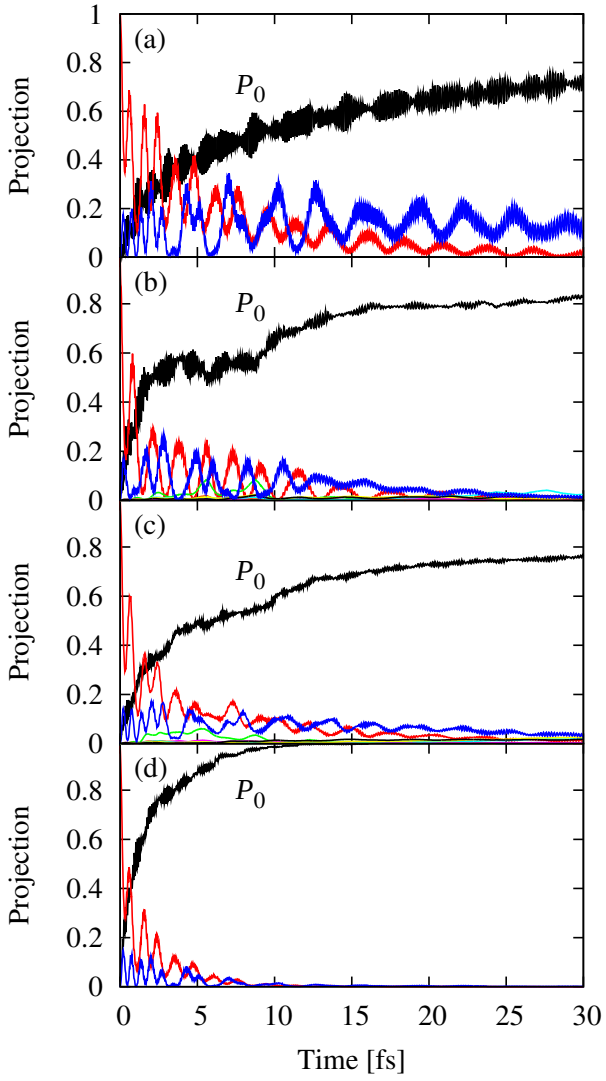

Figure 7.2 *Panel (a):* Projections $P_i = |\langle \epsilon_i | \psi \rangle|^2$ for neutral He, as a function of time, for the case where the stochastic terms are not included (unitary evolution). The solid black, dashed red, and dotted blue curves correspond to P_0, P_1, and P_8, respectively. *Panel (b):* Same for as panel (a), but with the inclusion of the interaction with the environment. *Panel (c):* Same for as panel (b), but averaged over five different runs, each with a different seed for the random number generator. *Panel (d):* Same as for panels (a)-(c), except the dynamics were calculated using the wave-packet collapse methodology of Eq. (7.7).

for the single-particle wavefunction $|\phi\rangle$.

Similarly to the case of He^+, we can make a connection with quantum measurement theory and study the decay of neutral He using Eq. (7.7). This is illustrated in Fig. 7.2(d). Here, however, we observe an important qualitative difference. In the wave-packet reduction formalism described by Eq. (7.7), after the apparatus "detects" the excitation, the system immediately collapses onto the ground state $|\epsilon_0\rangle$, *irrespective* of the interactions of the other states with the environment. In contrast, the non-unitary evolution of the stochastic Schrödinger Eq. (7.6) involves a constant process of *self-consistent* interaction with the reservoir. This implies that the frequency of small oscillations is unchanged in the wave-packet reduction formalism, while they change in time during dynamical interaction with the environment as described by Eq. (7.6). Clearly, one could introduce this effect into the wave-packet reduction Eq. (7.7), but at a non-trivial complexity cost, while the stochastic Schrödinger Eq. (7.6) contains it naturally.

In summary, we have used Stochastic TD-CDFT to describe the interaction of an excited quantum system (He) with an external environment and its consequent decay into the ground state; a problem previously inaccessible via standard DFT methods. We have made a connection of this open quantum problem with quantum measurement theory thus showing that Stochastic TD-CDFT may find applications in quantum information theory of realistic systems.

ACKNOWLEDGEMENTS

We thank Y. Pershin for useful discussions and for pointing out Ref. 124 to us. This work has been supported by the Department of Energy grant DE-FG02-05ER46204.

Appendix A

The Ceperley-Alder correlation potential

The Ceperley-Alder correlation potential [33], as parametrized by Perdew and Zunger [34], is given by

$$V_{\rm c}(\mathbf{r}) = \begin{cases} \frac{\gamma}{(1+\beta_1\sqrt{r_{\rm s}}+\beta_2 r_{\rm s})} \frac{(1+\frac{7}{6}\beta_1\sqrt{r_{\rm s}}+\frac{4}{3}\beta_2 r_{\rm s})}{(1+\beta_1\sqrt{(r_{\rm s})}+\beta_2 r_{\rm s})} & \text{if } r_{\rm s} \geq a_0, \\ A\ln r_{\rm s} + B + C r_{\rm s}\ln r_{\rm s} + D r_{\rm s} & \text{if } r_{\rm s} < a_0, \end{cases} \tag{A.1}$$

where the Wigner-Seitz radius r_s is defined by $r_{\rm s} = (\frac{3}{4\pi}\frac{1}{n})^{\frac{1}{3}}$, and the parameters γ, β_1, β_2, C and D are given in Table A.

Table A.1 Parameters for the Ceperley-Alder correlation potential $V_{\rm c}$

Parameter	Value
γ	-0.1423
β_1	1.0529
β_2	0.3334
C	0.0020
D	-0.0116

Appendix B

An example of the ultra-nonlocality problem

We reproduce here an argument given by Giuliani and Vignale in Ref. 25. We begin by deriving the so-called zero-force theorem and observe that, via Newton's third law, the total force exerted by electron-electron interactions must vanish. Next we consider the total force exerted by the Hartree potential:

$$\int \mathrm{d}\mathbf{r}\, n(\mathbf{r},t) \int \mathrm{d}\mathbf{r}' n(\mathbf{r}',t) \nabla_{\mathbf{r}} \frac{1}{|\mathbf{r}-\mathbf{r}'|} \tag{B.1}$$

We note that $\nabla_{\mathbf{r}} \frac{1}{|\mathbf{r}-\mathbf{r}'|}$ is antisymmetric upon the interchange of $\mathbf{r}$ and $\mathbf{r}'$; hence, the expression in (B.1) is zero. Therefore, the total force due to the exchange-correlation potential must also vanish:

$$\int \mathrm{d}\mathbf{r}\, n(\mathbf{r},t) \nabla_{\mathbf{r}} V_{\mathrm{xc}}[n](\mathbf{r},t) = 0\,. \tag{B.2}$$

Now we consider the response of the system to a periodic external potential of the form $V(\mathbf{r},t) = V_1(\mathbf{r},\omega)\mathrm{e}^{-\mathrm{i}\omega t} + V_1^*(\mathbf{r},\omega)\mathrm{e}^{\mathrm{i}\omega t}$. The density is given by $n(\mathbf{r},t) = n_0(\mathbf{r}) + n_1(\mathbf{r},\omega)\mathrm{e}^{-\mathrm{i}\omega t} + n_1^*(\mathbf{r},\omega)\mathrm{e}^{\mathrm{i}\omega t}$, where $n(\mathbf{r})$ is the electronic density in the absence of the perturbing potential V_1. Similarly, we can expand $V_{\mathrm{xc}}(\mathbf{r},t) = V_{\mathrm{xc},0}(\mathbf{r}) + V_{\mathrm{xc},1}(\mathbf{r},\omega)\mathrm{e}^{-\mathrm{i}\omega t} + V_{\mathrm{xc},1}^*(\mathbf{r},\omega)\mathrm{e}^{\mathrm{i}\omega t}$.

With these definitions, we can write equation (B.2) in the form

$$\int \mathrm{d}\mathbf{r}\, n_0(\mathbf{r})\nabla_{\mathbf{r}} V_{\mathrm{xc},1}(\mathbf{r},\omega) + \int \mathrm{d}\mathbf{r}\, n_1(\mathbf{r},\omega)\nabla_{\mathbf{r}} V_{\mathrm{xc},0}(\mathbf{r}) = 0\,. \tag{B.3}$$

If we write the first-order correction to V_{xc} in the form

$$V_{\mathrm{xc},1}(\mathbf{r},\omega) = \int \mathrm{d}\mathbf{r}'\, f_{\mathrm{xcL}}(\mathbf{r},\mathbf{r}',\omega) n_1(\mathbf{r}',\omega)\,, \tag{B.4}$$

where f_{xcL} is called the longitudinal exchange-correlation kernel, then integrating (B.2) by parts yields

$$\int \mathrm{d}\mathbf{r}\, (\nabla_{\mathbf{r}} n_0(\mathbf{r}))\, f_{\mathrm{xcL}}(\mathbf{r},\mathbf{r}',\omega) = \nabla_{\mathbf{r}'} V_{\mathrm{xc},0}(\mathbf{r}')\,, \tag{B.5}$$

or, equivalently,

$$\int \mathrm{d}\mathbf{r}' f_{\mathrm{xcL}}(\mathbf{r},\mathbf{r}',\omega)\, (\nabla_{\mathbf{r}'} n_0(\mathbf{r}')) = \nabla_{\mathbf{r}} V_{\mathrm{xc},0}(\mathbf{r})\,. \tag{B.6}$$

This is the zero-force theorem.

Now, consider a uniform electron gas, perturbed by a sinusoidal potential of wavevector $\mathbf{q}$. The ground state density $n_0(\mathbf{r})$ is given by

$$n_0(\mathbf{r}) = \bar{n}(1 + \gamma\cos(\mathbf{q}\cdot\mathbf{r})) \tag{B.7}$$

where the amplitude of the modulation γ is much less than 1. We next expand f_{xcL} in powers of γ, so that

$$f_{\mathrm{xcL}}(\mathbf{r},\mathbf{r}',\omega) = f^h_{\mathrm{xcL}}(|\mathbf{r}-\mathbf{r}'|,\omega) + \gamma f^{(1)}_{\mathrm{xcL}}(\mathbf{r},\mathbf{r}',\omega) + O(\gamma^2)\,, \tag{B.8}$$

where f^h_{xcL} is the longitudinal exchange-correlation kernel for the case of uniform density. Therefore, at zero frequency, equation (B.4) implies

$$V_{\mathrm{xc},0}(\mathbf{r}) = \gamma\bar{n}\int \mathrm{d}\mathbf{r}' f^{\mathrm{h}}_{\mathrm{xcL}}(\mathbf{r},\mathbf{r}',0)\cos(\mathbf{q}\cdot\mathbf{r}')\,. \tag{B.9}$$

We now *assume* that f_{xcL} has an effective range of less than $1/q$, and a typical strength of $q f_{\mathrm{xcL}}(q,0)$ so that

$$\begin{aligned} V_{\mathrm{xc},0}(\mathbf{r}) &\approx \gamma\bar{n}\left(\int \mathrm{d}\mathbf{r}' f^{\mathrm{h}}_{\mathrm{xcL}}(\mathbf{r},\mathbf{r}',0)\right)\cos(\mathbf{q}\cdot\mathbf{r}) \\ &= \gamma\bar{n} f^{\mathrm{h}}_{\mathrm{xcL}}(q,0)\cos(\mathbf{q}\cdot\mathbf{r})\,. \end{aligned} \tag{B.10}$$

The zero-force theorem in the form of equation (B.6), along with equations (B.7), (B.8), and (B.10) imply that

$$\int \mathrm{d}\mathbf{r}' f_{\mathrm{xcL}}^{(1)}(\mathbf{r},\mathbf{r}',\omega)\nabla_{\mathbf{r}'}\bar{n} = \bar{n}\left[f_{\mathrm{xcL}}^{\mathrm{h}}(q,0) - f_{\mathrm{xcL}}^{\mathrm{h}}(q,\omega)\right]\nabla_{\mathbf{r}}\cos(\mathbf{q}\cdot\mathbf{r})\,. \tag{B.11}$$

The right-hand side of this equation is clearly nonzero; however, the left-hand side must be zero, since the gradient of the constant $\bar{n}$ is zero.

This contradiction comes about as a result of our assumption that f_{xcL} is short-range. In fact, a local expansion of f_{xcL} does not exist; that is, f_{xcL} is inherantly long-range.

A local expansion in terms of the current density does not suffer from this problem. Vignale and Kohn [42] derived an expansion for $f_{\mathrm{xcL}}(\mathbf{q},\mathbf{k})$ that is local in the current density, and is analytic for small k, where $f_{\mathrm{xcL}}(\mathbf{q},\mathbf{k})$ is the Fourier transform of $f_{\mathrm{xcL}}(\mathbf{r},\mathbf{r}',\omega)$. In contrast, the expansion of $f_{\mathrm{xcL}}(\mathbf{q},\mathbf{k},\omega)$ in terms of the density is singular as $\mathbf{k}\to 0$. This means that, in principle, any frequency-dependent functional of the *density only* must be incorrect, although in practice, there exist regimes where frequency-dependent density functionals work reasonably well [25].

Appendix C

The Conti-Vignale interpolation formula for the electronic viscosity

The Conti-Vignale interpolation formula for the electronic viscosity η is given by [46]

$$\eta \approx \begin{cases} \left(60 r_{\mathrm{s}}^{-3/2} + c_1 r_{\mathrm{s}}^{-1} + c_2 r_{\mathrm{s}}^{-2/3} + c_3 r_{\mathrm{s}}^{-1/3}\right)^{-1} n & \text{in 3 dimensions} \\ \left[\left(\frac{r_s^2}{6\pi} \ln \sqrt{\frac{2}{r_{\mathrm{s}}}} + c_0 r_{\mathrm{s}}^2\right)^{-1} + c_1 r_{\mathrm{s}}^{-2} + c_2 r_{\mathrm{s}}^{-1/2} + c_3\right]^{-1} n & \text{in 2 dimensions,} \end{cases} \tag{C.1}$$

where the values of c_1, and c_2 are given in Table C, and we have again made use of the Wigner-Seitz radius $r_{\mathrm{s}} = (\frac{3}{4\pi}\frac{1}{n})^{\frac{1}{3}}$.

The bulk viscosity ζ is set to zero, since it is in general much smaller than the dynamic viscosity η.

Table C.1 Parameters for η using the estimate of Conti *et al.*.

Parameter	Value	
	2D	3D
c_0		0.25
c_1	80	21
c_2	-40	23
c_3	62	13

Bibliography

[1] P. Hohenberg and W. Kohn, Phys. Rev. **136**, B864 (1964).

[2] W. Kohn and L. Sham, Phys. Rev. **140**, A1133 (1965).

[3] E. G. Emberly and G. Kirczenow, Phys. Rev. B **58**, 10911 (1998).

[4] M. Di Ventra, S. T. Pantelides, and N. D. Lang, Phys. Rev. Lett. **84**, 979 (2000).

[5] Y. Xue, S. Datta, and M. A. Ratner, J. Chem. Phys. **115**, 4292 (2001).

[6] J. Taylor, H. Guo, and J. Wang, Phys. Rev. B **63**, 245407 (2001).

[7] P. S. Damle, A. W. Ghosh, and S. Datta, Phys. Rev. B **64**, 201403(R) (2001).

[8] M. Brandbyge, J.-L. Mozos, P. Ordejón, J. Taylor, and K. Stokbro, Phys. Rev. B **65**, 165401 (2002).

[9] J. Heurich, J. C. Cuevas, W. Wenzel, and G. Schön, Phys. Rev. Lett. **88**, 256803 (2002).

[10] J. J. Palacios, A. J. Pérez-Jiménez, E. Louis, E. SanFabián, and J. A. Vergés, Phys. Rev. B **66**, 035322 (2002).

[11] A. Pecchia and A. D. Carlo, Rep. Prog. Phys. **67**, 1497 (2004).

[12] A. R. Rocha, V. M. Garc´ia-Suárez, S. Bailey, C. Lambert, J. Ferrer, and S. Sanvito, Phys. Rev. B **73**, 085414 (2006).

[13] M. Di Ventra and T. N. Todorov, J. Phys.: Cond. Matt. **16**, 8025 (2004).

[14] R. Baer, T. Seideman, S. Ilani, and D. Neuhauser, J. Chem. Phys. **120**, 3387 (2004).

[15] G. Stefanucci and C.-O. Almbladh, Phys. Rev. B **69**, 195318 (2004).

[16] A. P. Horsfield, D. R. Bowler, A. J. Fisher, T. N. Todorov, and C. G. Sánchez, J. Phys.: Condens. Matter **16**, 8251 (2004).

[17] S. Kurth, G. Stefanucci, C.-O. Almbladh, A. Rubio, and E. K. U. Gross, Phys. Rev. B **72**, 035308 (2005).

[18] K. Burke, R. Car, and R. Gebauer, Phys. Rev. Lett. **94**, 146803 (2005).

[19] Y. Zhu, J. Maciejko, T. Ji, H. Guo, and J. Wang, Phys. Rev. B **71**, 075317 (2005).

[20] J. N. Pedersen and A. Wacker, Phys. Rev. B **72**, 195330 (2005).

[21] X. Qian, J. Li, X. Lin, and S. Yip, Phys. Rev. B **73**, 035408 (2006).

[22] C. G. Sánchez, M. Stamenova, S. Sanvito, D. R. Bowler, A. P. Horsfield, and T. N. Todorov, J. Chem. Phys. **124**, 214708 (2006).

[23] R. Shankar, *Principles of Quantum Mechanics* (Plenum Press, New York, 1980), 2nd ed.

[24] M. Levy, Proc. Natl. Acad. Sci. USA **76**, 6062 (1979).

[25] G. F. Giuliani and G. Vignale, *Quantum Theory of the Electron Liquid* (Cambridge University Press, 2005).

[26] M. Levy, Phys. Rev. A **26**, 1200 (1982).

[27] P. H. Dederichs and R. Zeller, Phys. Rev. B **28**, 5462 (1983).

[28] D. G. Anderson, J. Assoc. Comput. Mach. **12**, 547 (1965).

[29] V. Eyert, J. Comput. Phys. **123**, 271 (1996).

[30] J. C. Slater, Phys. Rev. **81**, 385 (1951).

[31] T. B. Pedersen, Master's thesis, Technical University of Denmark (2000).

[32] P. A. M. Dirac, Proc. Cambridge Phil. Soc. **26**, 376 (1930).

[33] D. M. Ceperley and B. J. Alder, Phys. Rev. Lett. **45**, 566 (1980).

[34] J. P. Perdew and A. Zunger, Phys. Rev. B **23**, 5048 (1981).

[35] J. P. Perdew, K. Burke, and M. Ernzerhof, Phys. Rev. Lett. **77**, 3865 (1996).

[36] R. Landauer, IBM J. Res. Dev. **1**, 223 (1957).

[37] D. R. Hamann, Phys. Rev. B **40**, 2980 (1989).

[38] R. van Leeuwen, Phys. Rev. Lett. **82**, 3863 (1999).

[39] E. Runge and E. K. U. Gross, Phys. Rev. Lett. **52**, 997 (1984).

[40] A. Zangwill and P. Soven, Phys. Rev. Lett. **45**, 204 (1980).

[41] G. Vignale, Phys. Lett. A **209**, 206 (1995).

[42] G. Vignale and W. Kohn, Phys. Rev. Lett. **77**, 2037 (1996).

[43] N. Sai, M. Zwolak, G. Vignale, and M. Di Ventra, Phys. Rev. B **75**, 115410 (2007).

[44] G. Vignale, C. A. Ullrich, and S. Conti, Phys. Rev. Lett. **79**, 4878 (1997).

[45] R. Nifosi, S. Conti, and M. P. Tosi, Phys. Rev. B **58**, 12758 (1998).

[46] S. Conti and G. Vignale, Phys. Rev. B **60**, 7966 (1999).

[47] C. Moler and C. Van Loan, SIAM Review **45**, 3 (2003).

[48] H. Tal-Ezer and R. Kosloff, J. Chem. Phys. **81**, 3967 (1984).

[49] C. Leforestier, R. H. Bisseling, C. Cerjan, M. D. Feit, R. Friesner, A. Guldberg, A. Hammerich, G. Jolicard, W. Karrlein, H. Meyer, et al., J. Comput. Phys. **94**, 59 (1990).

[50] R. S. Varga, *Matrix Iterative Analysis* (Prentice Hall, Inc, Englewood Cliffs, NJ, 1962).

[51] E. W. Weisstein, *Gershgorin circle theorem* (2006), from Mathworld – a Wolfram Web Resource, URL `http://mathworld.wolfram.com/GershgorinCircleTheorem.html`.

[52] M. Büttiker, Y. Imry, R. Landauer, and S. Pinhas, Phys. Rev. B **31**, 6207 (1985).

[53] Y. Imry, in *Directions in Condensed Matter Physics*, edited by G. Grinstein and G. Mazenko (World Scientific, Singapore, 1986), p. 101.

[54] R. Landauer, Z. Phys. B **68**, 217 (1987).

[55] N. W. Ashcroft and N. D. Mermin, *Sold State Physics* (W.B. Saunders, Philadelphia, 1976).

[56] T. Todorov, J. Phys.: Condens. Matter **14**, 3049 (2002).

[57] J. Lagerqvist, Y.-C. Chen, and M. Di Ventra, Nanotechnology **15**, S459 (2004).

[58] N. Agräit, A. L. Yeyati, and J. M. van Ruitenbeek, Phys. Rep. **377**, 81 (2003).

[59] R. Landauer, J. Phys.: Condens. Matter **1**, 8099 (1989).

[60] R. Landauer, Physica Scipta **T42**, 110 (1992).

[61] M. C. Payne, J. Phys.: Condens. Matter **1**, 4931 (1984).

[62] A. Zangwill and P. Soven, Phys. Rev. B **24**, 4121 (1981).

[63] B. G. Briner, R. M. Feenstra, T. P. Chin, and J. M. Woodall, Phys. Rev. B **54**, 5283 (1996).

[64] M. A. Eriksson, R. G. Beck, M. Topinka, J. A. Katine, R. M. Westervelt, K. L. Campman, and A. C. Gossard, Appl. Phys. Lett. **69**, 671 (1996).

[65] R. M. Feenstra and B. R. Briner, Supplattices & Microstructures **23**, 699 (1998).

[66] M. A. Topinka, B. J. LeRoy, S. E. J. Shaw, E. J. Heller, R. M. Westervelt, K. D. Maranowski, and A. C. Gossard, Science **289**, 2323 (2000).

[67] Y. Blanter and M. Büttiker, Phys. Rep. **336**, 1 (2000).

[68] S. Camalet, J. Lehmann, S. Kohler, and P. Hänggi, Phys. Rev. Lett. **90**, 210602 (2003).

[69] Y.-C. Chen and M. Di Ventra, Phys. Rev. B **67**, 153304 (2003).

[70] M. J. Montgomery, T. N. Todorov, and A. P. Sutton, J. Phys.: Condens. Matter **14**, 5377 (2002).

[71] Y.-C. Chen, M. Zwolak, and M. Di Ventra, Nano Lett. **3**, 1691 (2003).

[72] T. Frederiksen, M. Brandbyge, N. Lorente, and A.-P. Jauho, Phys. Rev. Lett. **93**, 256601 (2004).

[73] M. Di Ventra, S. Pantelides, and N. Lang, Phys. Rev. Lett. **88**, 046801 (2002).

[74] Z. Yang, M. Chshiev, M. Zwolak, Y.-C. Chen, and M. Di Ventra, Phys. Rev. B **71**, 041402(R) (2005).

[75] N. D. Lang, Phys. Rev. B **36**, 8173 (1987).

[76] T. N. Todorov, Phil. Mag. B **89**, 1577 (1999).

[77] N. S. Wingreen, A.-P. Jauho, and Y. Meir, Phys. Rev. B **48**, 8487 (1993).

[78] M. Grifoni and P. Hänggi, Phys. Rep. **304**, 229 (1998).

[79] M. Büttiker00, J. Low Temp. Phys. **118**, 519 (2000).

[80] N. Bushong, N. Sai, and M. Di Ventra, Nano Lett. **5**, 2569 (2005).

[81] P. Delaney and J. C. Greer, Phys. Rev. Lett. **93**, 036805 (2004).

[82] M. Koentopp, K. Burke, and F. Evers, Phys. Rev. B **73**, 121402(R) (2006).

[83] P. Bokes, J. Jung, and R. W. Godby, ArXiv Condensed Matter e-prints (2006), `arXiv:cond-mat/0604317v1`.

[84] C. Toher, A. Filippetti, S. Sanvito, and K. Burke, Phys. Rev. Lett. **95**, 146402 (2005).

[85] S.-H. Ke, H. U. Baranger, and W. Yang, ArXiv Condensed Matter e-prints (2006), `arXiv:cond-mat/0609637v1`.

[86] B. Muralidharan, A. W. Ghosh, and S. Datta, Phys. Rev. B **73**, 155410 (2006).

[87] C.-L. Cheng, J. S. Evans, and T. V. Voorhis, Phys. Rev. B **74**, 155112 (2006).

[88] S. N. Laboratories, we have modified the `socorro` code in order to include evolution in time.

[89] R. W. Hockney, in *Methods in Computational Physics*, edited by B. Alder, S. Ferbach, and M. Rotenberg (Academic Press, Inc., New York, 1970), vol. 9, p. 135.

[90] N. D. Lang and M. Di Ventra, Phys. Rev. B **68**, 157301 (2003).

[91] M. Di Ventra and N. D. Lang, Phys. Rev. B **65**, 045402 (2001).

[92] P. C. Martin and J. Schwinger, Phys. Rev. **115**, 1342 (1959).

[93] I. Tokatly and O. Pankratov, Phys. Rev. B **60**, 15550 (1999).

[94] I. V. Tokatly, Phys. Rev. B **71**, 165104 (2005).

[95] R. D'Agosta and M. Di Ventra, J. Phys.: Condens. Matter **18**, 11059 (2006).

[96] K.-F. Berggren, A. F. Sadreev, and A. A. Starikov, Phys. Rev. E **66**, 016219 (2002).

[97] I. V. Zozoulenko and T. Blomquist, Phys. Rev. B **67**, 085320 (2002).

[98] L. D. Landau and E. M. Lifshitz, *Fluid Mechanics*, vol. 6 of *Course of Theoretical Physics* (Pergamon Press, NY, 1987), 2nd ed.

[99] H. Mera, P. Bokes, and R. W. Godby, Phys. Rev. B **72**, 085311 (2005).

[100] A. Prociuk, B. V. Kuiken, and B. D. Dunietz, J. Chem. Phys. **125**, 204717 (2006).

[101] U. Frisch, *Turbulence* (Cambridge University Press, Cambridge, 1995).

[102] N. Sai, N. Bushong, R. Hatcher, and M. Di Ventra, Phys. Rev. B **75**, 115410 (2007).

[103] S. Popinet, J. Comput. Phys. **190**, 572 (2003).

[104] R. D'Agosta, N. Sai, and M. Di Ventra, Nano Lett. **6**, 2935 (2006).

[105] Z. F. Huang, B. Q. Xu, Y.-C. Chen, M. Di Ventra, and N. J. Tao, Nano Lett. **6**, 1240 (2006).

[106] M. Tsutsui, S. Kurokawa, and A. Sakai, Nanotechnology **17**, 5334 (2006).

[107] R. H. M. Smit, C. Untiedt, and J. M. van Ruitenbeek, Nanotechnology **15**, S472 (2004).

[108] E. Madelung, Z. Phys. **40**, 322 (1926).

[109] F. Bloch, Z. Phys. **81**, 363 (1933).

[110] N. Bushong, J. Gamble, and M. Di Ventra, Nano Lett. **7**, 1789 (2007).

[111] J. C. Gallop, *SQUIDS, the Josephson effects and superconducting electroncs* (IOP Publishing Ltd., 1991).

[112] R. D'Agosta, M. Di Ventra, and G. Vignale, Phys. Rev. B (in press) (2007).

[113] M. B. Ketchen, M. Bhushan, S. B. Kaplan, and W. J. Gallagher, IEEE Trans. Magn. **MAG-27**, 3005 (1991).

[114] J. R. Kirtley, M. B. Ketchen, C. C. Tsuei, J. Z. Sun, W. J. Gallagher, Lock See Yu-Jahnes, A. Gupta, K. G. Stawiasz, and S. J. Wind, IBM J. Res. Dev. **39**, 655 (1995).

[115] C. Veauvy, K. Hasselbach, and D. Mailly, Phys. Rev. B **70**, 214513 (2004).

[116] R. B. Dinner, M. R. Beasley, and K. A. Moler, Rev. Sci. Instrum. 76, 103702 (2005) **76**, 103702 (2005).

[117] J. Liu, A. Harris, and N. Kanwisher, Nat. Neurosci. **5**, 910 (2002).

[118] S. K. Ghosh and A. K. Dhara, Phys. Rev. A **38**, 1149 (1988).

[119] N. G. V. Kampen, *Stochastic Processes in Physics and Chemistry* (Elsevier, 2006), Revised and enlarged ed.

[120] A. Alavi, J. Chem. Phys. **113**, 7735 (2000).

[121] E. J. Bylaska, M. Valiev, R. Kawai, and J. H. Weare, Comput. Phys. Commun. **143**, 11 (2002).

[122] W. Zurek, Rev. Mod. Phys. **75**, 715 (2003).

[123] M. Schlosshauer, Rev. Mod. Phys. **76**, 1267 (2004).

[124] J. Dalibard, Y. Castin, and K. Mølmer, Phys. Rev. Lett. **68**, 580 (1992).

[125] O. Sugino and Y. Miyamoto, Phys. Rev. B **59**, 2579 (1999).